Higher-order modes of vacuum-clad ultrathin optical fibers

Fam Le Kien and Thomas Busch

Quantum Systems Unit, Okinawa Institute of Science and Technology Graduate University, Onna, Okinawa 904-0495, Japan

Viet Giang Truong

Light-Matter Interactions Unit, Okinawa Institute of Science and Technology Graduate University, Onna, Okinawa 904-0495, Japan

Síle Nic Chormaic

Light-Matter Interactions Unit, Okinawa Institute of Science and Technology Graduate University, Onna, Okinawa 904-0495, Japan
and School of Chemistry and Physics, University of KwaZulu-Natal, Durban, KwaZulu-Natal 4001, South Africa

We present a systematic treatment of higher-order modes of vacuum-clad ultrathin optical fibers. We show that, for a given fiber, the higher-order modes have larger penetration lengths, larger effective mode radii, and larger fractional powers outside the fiber than the fundamental mode. We calculate, both analytically and numerically, the Poynting vector, propagating power, energy, angular momentum, and helicity (or chirality) of the guided light. The axial and azimuthal components of the Poynting vector can be negative with respect to the direction of propagation and the direction of phase circulation, respectively, depending on the position, the mode type, and the fiber parameters. The orbital and spin parts of the Poynting vector may also have opposite signs in some regions of space. We show that the angular momentum per photon decreases with increasing fiber radius and increases with increasing azimuthal mode order. The orbital part of angular momentum of guided light depends not only on the phase gradient but also on the field polarization, and is positive with respect to the direction of the phase circulation axis. Meanwhile, depending on the mode type, the spin and surface parts of angular momentum and the helicity of the field can be negative with respect to the direction of the phase circulation axis.

I. INTRODUCTION

Near-field optics using optical fibers is currently a highly active and productive area of research that has implications for optical communication, sensing, computing, and even quantum information. Its main tools are so-called nanofibers, which are optical fibers that are tapered to a diameter comparable to or smaller than the wavelength of light [1–3]. The essence of the tapering technique is to heat and pull a single-mode optical fiber to a very small thickness, while maintaining the taper condition adiabatically [1–4]. Due to the tapering, the original core almost vanishes and the refractive indices that determine the guiding properties of the tapered fiber are those of the original silica cladding and the surrounding vacuum. Thus, these fibers can be treated as very thin vacuum-clad silica-core fibers.

In a vacuum-clad nanofiber, the guided field penetrates an appreciable distance into the surrounding medium and appears as an evanescent wave carrying a significant fraction of the power and having a complex polarization pattern [5–7]. These fibers offer high transmission and strong confinement of guided light in the transverse plane of the fiber. This confinement allows one to efficiently couple guided light to emitters placed on or near the fiber surface. Such fibers are therefore versatile tools for coupling light and matter and have a wide range of potential practical applications [8,9].

For example, they have been used for trapping atoms [10–12], for probing atoms [13–19], molecules [20], quantum dots [21], and color centers in nanodiamonds [22,23], and for mechanical manipulation of small particles [24–26]. Due to the lack of cutoff as well as the possession of a small mode area and a simple mode structure, the fundamental HE_{11} mode has been exploited in most studies to date.

However, tapered fibers can also be fabricated with slightly larger diameters and/or larger refractive indices so that they can support not only the fundamental HE_{11} mode but also several higher-order modes. Compared to the HE_{11} mode, the higher-order modes have larger cutoff size parameters and more complex intensity, phase, and polarization distributions. In addition, the higher-order modes can have larger angular momentum compared to the HE_{11} mode. For ease of reference, the micro- and nanofibers that can support the fundamental mode and several higher-order modes are called ultrathin fibers in this paper.

Theoretical studies have shown that ultrathin fibers with higher-order modes can be used to trap, probe, and manipulate atoms, molecules, and particles [27–33]. The excitation of higher-order modes has been studied [34,35], and the production of ultrathin fibers for higher-order mode propagation with high transmission has been demonstrated [4,36,37]. First experimental studies on the interaction between higher-order modes and atoms [38] or particles [39,40] have also been reported.

Despite increased interest in higher-order modes of ultrathin fibers, systematic treatments for the basic properties of light fields in such modes do not exist. Although the full and exact fiber theory [41] is applicable also to ultrathin fibers, deep understanding can only be reached only by

combining a systematic and comprehensive analysis with detailed numerical calculations for fibers with parameters in the range of experimental interest. The purpose of this work is to present such a systematic treatment. We show that, for a given fiber, the higher-order modes have larger penetration lengths, larger effective mode radii, and larger fractional powers outside the fiber than the fundamental mode. We calculate analytically and numerically the Poynting vector, propagating power, energy, angular momentum, and helicity (or chirality) of guided light. The numerical results for these characteristics are derived from the corresponding analytical results.

The paper is organized as follows. In Sec. II we briefly review the theory of guided modes of optical fibers and present the results of numerical calculations for the propagation constants and penetration lengths of the modes of fibers with the parameters in the range of experimental interest. Section III is devoted to the study of the electric intensity distribution and the effective mode radius. In Sec. IV we calculate the Poynting vector, propagating power, and energy per unit length, and examine the orbital and spin parts of the Poynting vector. Section V is devoted to the study of angular momentum of guided light and its orbital, spin, and surface parts. In Sec. VI we calculate the helicity and the associated chirality of guided light. Our conclusions are given in Sec. VII. In order to focus on the underlying physics of guided light in higher-order modes, we put the lengthy mathematical expressions for the mode functions and some analytical results in the appendixes.

II. GUIDED MODES OF OPTICAL FIBERS

In this section, we first briefly review the theory of guided modes of optical fibers and then calculate the propagation constants and evanescent-wave penetration lengths of the fundamental mode and higher-order modes of ultrathin fibers with parameters in the range of experimental interest.

For this we consider the model of a step-index fiber that is a dielectric cylinder of radius a and refractive index n_1, surrounded by an infinite background medium of refractive index n_2, where $n_2 < n_1$. We use Cartesian coordinates $\{x,y,z\}$, where z is the coordinate along the fiber axis, and also cylindrical coordinates $\{r,\varphi,z\}$, where r and φ are the polar coordinates in the fiber transverse plane xy.

For a guided light field of frequency ω (free-space wavelength $\lambda = 2\pi c/\omega$ and free-space wave number $k = \omega/c$), the propagation constant β is determined by the fiber eigenvalue equation [41]

$$\left[\frac{J'_l(ha)}{haJ_l(ha)} + \frac{K'_l(qa)}{qaK_l(qa)}\right]\left[\frac{n_1^2 J'_l(ha)}{haJ_l(ha)} + \frac{n_2^2 K'_l(qa)}{qaK_l(qa)}\right]$$
$$= l^2\left(\frac{1}{h^2 a^2} + \frac{1}{q^2 a^2}\right)^2 \frac{\beta^2}{k^2}. \quad (1)$$

Here, we have introduced the parameters $h = (n_1^2 k^2 - \beta^2)^{1/2}$ and $q = (\beta^2 - n_2^2 k^2)^{1/2}$, which characterize the scales of the spatial variations of the field inside and outside the fiber, respectively. The integer index $l = 0,1,2,\dots$ is the azimuthal mode order, which determines the helical phase front and the associated phase gradient in the fiber transverse plane. The notations J_l and K_l stand for the Bessel functions of the
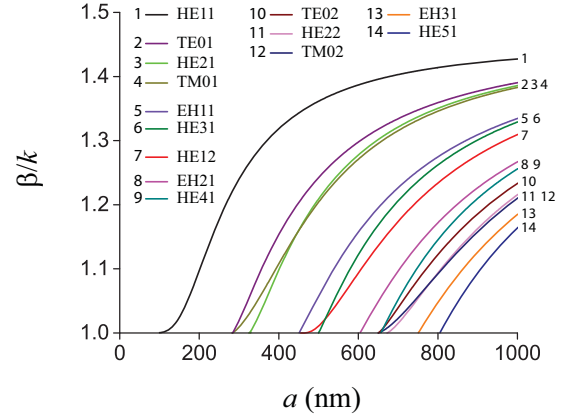

FIG. 1. Propagation constant β, normalized to the free-space wave number k, as a function of the fiber radius a. The wavelength of the light is chosen to be $\lambda = 780$ nm. The refractive index of the fiber is $n_1 = 1.4537$ and of the surrounding medium is $n_2 = 1$.

first kind and the modified Bessel functions of the second kind, respectively. The notations $J'_l(x)$ and $K'_l(x)$ stand for the derivatives of $J_l(x)$ and $K_l(x)$ with respect to the argument x.

For $l \geqslant 1$, the eigenvalue equation (1) leads to hybrid HE and EH modes [41], for which the eigenvalue equations are given by Eqs. (A1) and (A2) in Appendix A. We label these modes as HE_{lm} and EH_{lm}, where $l = 1,2,\dots$ is the azimuthal and $m = 1,2,\dots$ the radial mode orders. The radial mode order m implies that the HE_{lm} or EH_{lm} mode is the mth solution to the corresponding eigenvalue equation.

For $l = 0$, the eigenvalue equation (1) leads to TE and TM modes [41], for which the eigenvalue equations are given by Eqs. (A4) and (A5) in Appendix A. We label these modes as TE_{0m} and TM_{0m}, where again $m = 1,2,\dots$ is the radial mode order and the subscript 0 implies that the azimuthal mode order of each mode is $l = 0$.

We are interested in vacuum-clad ultrathin fibers, which can support not only the fundamental HE_{11} mode but also several higher-order modes in the optical region. For this we plot in Fig. 1 the propagation constant β for the HE_{11} mode and a large number of higher-order modes as a function of the fiber radius a for a wavelength of light that is chosen to be $\lambda = 780$ nm. The fiber is assumed to be made of silica, with a refractive index $n_1 = 1.4537$, and the surrounding medium is air or vacuum, with a refractive index $n_2 = 1$. One can see that the first two higher-order modes, TE_{01} and TM_{01}, appear when $a \simeq 283$ nm, and the next higher-order mode, HE_{21}, appears when $a \simeq 325$ nm. It is clear that the number of modes supported by the fiber increases with increasing fiber radius a. The numerical results presented in Fig. 1 are in agreement with the results of Refs. [28,36,38]. We note that the propagation constant was calculated in Refs. [28,38] for just a few modes and was plotted in Refs. [28,36,38] as a function of the fiber size parameter. We emphasize that the fiber size parameter is not a rigorous scaling parameter because the fiber material is dispersive.

Outside the fiber, the guided modes are evanescent waves in the radial direction r. The penetration depth is characterized by the parameter $\Lambda = 1/q$, which we show for the HE_{11} mode and several higher-order modes as a function of the fiber radius a in Fig. 2. One can see that, near to the cutoffs,
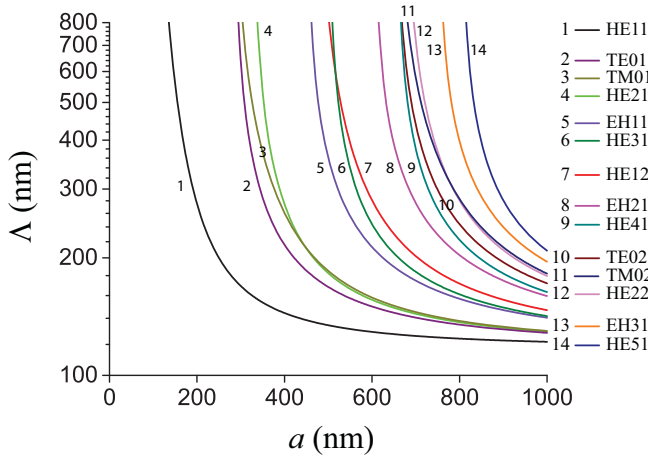
FIG. 2. Penetration length $\Lambda = 1/q$ as a function of the fiber radius a. The parameters used are the same as for Fig. 1.

the penetration length Λ is large, that is, the field is not tightly confined inside the fiber. Furthermore, when the fiber radius a increases, the penetration length decreases to the limiting value $\Lambda_{\min} = 1/(k\sqrt{n_1^2 - n_2^2})$. In general, for a given fiber, the higher-order modes have larger penetration lengths than the HE_{11} mode.

We will next discuss the mode functions [41]. For this we will write the electric and magnetic components of the field in the form $\mathbf{E} = (\mathcal{E}e^{-i\omega t} + \text{c.c.})/2$ and $\mathbf{H} = (\mathcal{H}e^{-i\omega t} + \text{c.c.})/2$, where $\mathcal{E}$ and $\mathcal{H}$ are spatial envelope functions, which obey the Helmholtz equation. They are the mode functions we are interested in and, for a guided mode with a propagation constant β and an azimuthal mode order l, we can write them as $\mathcal{E} = \mathbf{e}e^{i\beta z+il\varphi}$ and $\mathcal{H} = \mathbf{h}e^{i\beta z+il\varphi}$. Here, $\mathbf{e}$ and $\mathbf{h}$ are the reduced mode profile functions of the electric and magnetic components of the field, respectively, and β and l can take not only positive but also negative values. In the following we will consider hybrid modes, TE modes, and TM modes separately.

A. Hybrid modes

1. Quasicircularly polarized hybrid modes

In this section, we consider quasicircularly polarized hybrid HE and EH modes. For convenience, we use the notations $\beta > 0$ and $l > 0$ for the propagation constant and the azimuthal mode order, respectively. We introduce the index $f = +1$ or -1 (or simply $f = +$ or $-$) for the positive ($+\hat{\mathbf{z}}$) or negative ($-\hat{\mathbf{z}}$) propagation direction, which leads to the corresponding propagation phase factor of $e^{i\beta z}$ or $e^{-i\beta z}$. We also introduce the index $p = +1$ or -1 (or simply $p = +$ or $-$) for the counterclockwise or clockwise phase circulation, corresponding to the azimuthal phase factor of $e^{il\varphi}$ or $e^{-il\varphi}$. The index $p = +$ or $-$ also indicates that the central phase circulation axis is $+\hat{\mathbf{z}}$ or $-\hat{\mathbf{z}}$. We can label quasicircularly polarized hybrid modes by the mode index $\mu = (flp)$, which can also be extended to include the mode type, HE or EH, and the radial mode order, m, when necessary.

We choose a notation in which we decompose an arbitrary vector $\mathbf{V} = \hat{\mathbf{r}}V_r + \hat{\boldsymbol{\varphi}}V_\varphi + \hat{\mathbf{z}}V_z$ into the radial, azimuthal, and axial components denoted by the subscripts r, φ, and z. The

notations $\hat{\mathbf{r}} = \hat{\mathbf{x}}\cos\varphi + \hat{\mathbf{y}}\sin\varphi$, $\hat{\boldsymbol{\varphi}} = -\hat{\mathbf{x}}\sin\varphi + \hat{\mathbf{y}}\cos\varphi$, and $\hat{\mathbf{z}}$ stand for the unit basis vectors of the cylindrical coordinate system $\{r,\varphi,z\}$, with $\hat{\mathbf{x}}$ and $\hat{\mathbf{y}}$ being the unit basis vectors of the Cartesian coordinate system for the fiber transverse plane xy. The position vector in the fiber transverse plane is given by $\mathbf{r} = r\hat{\mathbf{r}} = x\hat{\mathbf{x}} + y\hat{\mathbf{y}}$.

In the cylindrical coordinates, the reduced mode profile functions $\mathbf{e}^{(flp)}(\mathbf{r})$ and $\mathbf{h}^{(flp)}(\mathbf{r})$ of the electric and magnetic components of a quasicircularly polarized hybrid mode with the propagation direction f, the azimuthal mode order l, and the phase circulation direction p are then given by

$$
\begin{aligned}
\mathbf{e}^{(flp)} &= \hat{\mathbf{r}}e_r + p\hat{\boldsymbol{\varphi}}e_\varphi + f\hat{\mathbf{z}}e_z, \\
\mathbf{h}^{(flp)} &= fp\hat{\mathbf{r}}h_r + f\hat{\boldsymbol{\varphi}}h_\varphi + p\hat{\mathbf{z}}h_z,
\end{aligned}
\tag{2}
$$

where the electric mode function components e_r, e_φ, and e_z and the magnetic mode function components h_r, h_φ, and h_z are given by Eqs. (A9)–(A12) for $\beta > 0$ and $l > 0$ in Appendix A. These mode function components depend explicitly on the azimuthal mode order l and implicitly on the radial mode order m. An important property of the mode functions is that the longitudinal components e_z and h_z are nonvanishing and in quadrature ($\pi/2$ out of phase) with the radial components e_r and h_r, respectively. In addition, the azimuthal components e_φ and h_φ are also nonvanishing and in quadrature with the radial components e_r and h_r, respectively. The electric and magnetic polarizations of hybrid modes are not of the TE and TM types. Note that the full mode functions for quasicircularly polarized hybrid modes are given by

$$
\mathcal{E}_{\text{circ}}^{(flp)} = \mathbf{e}^{(flp)}e^{if\beta z+ipl\varphi}, \quad \mathcal{H}_{\text{circ}}^{(flp)} = \mathbf{h}^{(flp)}e^{if\beta z+ipl\varphi}. \tag{3}
$$

2. Quasilinearly polarized hybrid modes

Quasilinearly polarized hybrid modes are linear superpositions of counterclockwise and clockwise quasicircularly polarized hybrid modes. The full mode functions of the electric and magnetic components of the guided field in a quasilinearly polarized hybrid mode (f,l,φ_{pol}) are given by [41]

$$
\begin{aligned}
\mathcal{E}_{\text{lin}}^{(fl\varphi_{\text{pol}})} &= \frac{1}{\sqrt{2}}\left(\mathcal{E}_{\text{circ}}^{(fl+)}e^{-i\varphi_{\text{pol}}} + \mathcal{E}_{\text{circ}}^{(fl-)}e^{i\varphi_{\text{pol}}}\right), \\
\mathcal{H}_{\text{lin}}^{(fl\varphi_{\text{pol}})} &= \frac{1}{\sqrt{2}}\left(\mathcal{H}_{\text{circ}}^{(fl+)}e^{-i\varphi_{\text{pol}}} + \mathcal{H}_{\text{circ}}^{(fl-)}e^{i\varphi_{\text{pol}}}\right).
\end{aligned}
\tag{4}
$$

Here, the phase angle φ_{pol} determines the orientation of the symmetry axes of the mode profile in the fiber transverse plane. In particular, the specific phase angle values $\varphi_{\text{pol}} = 0$ and $\pi/2$ define two orthogonal polarization profiles, one being symmetric with respect to the x axis and the other being the result of the rotation of the first one by an angle of $\pi/2l$ in the fiber transverse plane xy.

We can write

$$
\mathcal{E}_{\text{lin}}^{(fl\varphi_{\text{pol}})} = \mathbf{e}^{(fl\varphi_{\text{pol}})}e^{if\beta z}, \quad \mathcal{H}_{\text{lin}}^{(fl\varphi_{\text{pol}})} = \mathbf{h}^{(fl\varphi_{\text{pol}})}e^{if\beta z}, \tag{5}
$$

where $\mathbf{e}^{(fl\varphi_{\text{pol}})}$ and $\mathbf{h}^{(fl\varphi_{\text{pol}})}$ are the reduced mode profile functions of quasilinearly polarized hybrid modes and are

given as

$$\mathbf{e}^{(fl\varphi_{\mathrm{pol}})} = \frac{1}{\sqrt{2}}(\mathbf{e}^{(fl+)}e^{i(l\varphi-\varphi_{\mathrm{pol}})} + \mathbf{e}^{(fl-)}e^{-i(l\varphi-\varphi_{\mathrm{pol}})}),$$

$$\mathbf{h}^{(fl\varphi_{\mathrm{pol}})} = \frac{1}{\sqrt{2}}(\mathbf{h}^{(fl+)}e^{i(l\varphi-\varphi_{\mathrm{pol}})} + \mathbf{h}^{(fl-)}e^{-i(l\varphi-\varphi_{\mathrm{pol}})}). \quad (6)$$

Inserting Eqs. (2) into Eqs. (6) yields

$$\mathbf{e}^{(fl\varphi_{\mathrm{pol}})} = \sqrt{2}[\hat{\mathbf{r}}e_r \cos(l\varphi-\varphi_{\mathrm{pol}}) + i\hat{\boldsymbol{\varphi}}e_\varphi \sin(l\varphi-\varphi_{\mathrm{pol}})$$
$$+ f\hat{\mathbf{z}}e_z \cos(l\varphi-\varphi_{\mathrm{pol}})],$$

$$\mathbf{h}^{(fl\varphi_{\mathrm{pol}})} = \sqrt{2}[if\hat{\mathbf{r}}h_r \sin(l\varphi-\varphi_{\mathrm{pol}}) + f\hat{\boldsymbol{\varphi}}h_\varphi \cos(l\varphi-\varphi_{\mathrm{pol}})$$
$$+ i\hat{\mathbf{z}}h_z \sin(l\varphi-\varphi_{\mathrm{pol}})]. \quad (7)$$

In particular, we find, for $\varphi_{\mathrm{pol}} = 0$,

$$\mathbf{e}^{(fl,0)} = \sqrt{2}(\hat{\mathbf{r}}e_r \cos l\varphi + i\hat{\boldsymbol{\varphi}}e_\varphi \sin l\varphi + f\hat{\mathbf{z}}e_z \cos l\varphi),$$

$$\mathbf{h}^{(fl,0)} = \sqrt{2}(if\hat{\mathbf{r}}h_r \sin l\varphi + f\hat{\boldsymbol{\varphi}}h_\varphi \cos l\varphi + i\hat{\mathbf{z}}h_z \sin l\varphi),$$

$$(8)$$

and, for $\varphi_{\mathrm{pol}} = \pi/2$,

$$\mathbf{e}^{(fl,\pi/2)} = \sqrt{2}(\hat{\mathbf{r}}e_r \sin l\varphi - i\hat{\boldsymbol{\varphi}}e_\varphi \cos l\varphi + f\hat{\mathbf{z}}e_z \sin l\varphi),$$

$$\mathbf{h}^{(fl,\pi/2)} = \sqrt{2}(-if\hat{\mathbf{r}}h_r \cos l\varphi + f\hat{\boldsymbol{\varphi}}h_\varphi \sin l\varphi - i\hat{\mathbf{z}}h_z \cos l\varphi).$$

$$(9)$$

B. TE modes

We again label the propagation directions of TE modes by the index $f = +$ or $-$. The reduced mode profile functions of the electric and magnetic components of TE modes with the propagation directions f can be written as

$$\mathbf{e}^{(f)} = \hat{\boldsymbol{\varphi}}e_\varphi, \quad \mathbf{h}^{(f)} = f\hat{\mathbf{r}}h_r + \hat{\mathbf{z}}h_z, \quad (10)$$

where the mode function components e_φ, h_r, and h_z are given by Eqs. (A13)–(A16) for $\beta > 0$ in Appendix A. They depend implicitly on the radial mode order m. It is clear from Eqs. (10) that, for TE modes, we have $e_r^{(f)} = e_z^{(f)} = h_\varphi^{(f)} = 0$. The electric polarization of a TE mode is therefore linear and aligned along the azimuthal direction. Meanwhile, since h_r is $\pi/2$ out of phase with respect to h_z, the magnetic polarization of the mode is elliptical in the meridional rz plane, which contains the radial r axis and the fiber z axis. The full mode functions of TE modes are given by $\boldsymbol{\mathcal{E}}^{(f)} = \mathbf{e}^{(f)}e^{if\beta z}$ and $\boldsymbol{\mathcal{H}}^{(f)} = \mathbf{h}^{(f)}e^{if\beta z}$.

C. TM modes

We also label the propagation directions of TM modes by the index $f = +$ or $-$. The reduced mode profile functions of the electric and magnetic components of TM modes with the propagation directions f can be written as

$$\mathbf{e}^{(f)} = \hat{\mathbf{r}}e_r + f\hat{\mathbf{z}}e_z, \quad \mathbf{h}^{(f)} = f\hat{\boldsymbol{\varphi}}h_\varphi, \quad (11)$$

where the mode function components e_r, e_z, and h_φ are given by Eqs. (A17)–(A20) for $\beta > 0$ in Appendix A. They depend implicitly on the radial mode order m. It is clear from Eqs. (11) that, for TM modes, we have $e_\varphi^{(f)} = h_r^{(f)} = h_z^{(f)} = 0$. The magnetic polarization of a TM mode is therefore linear and

aligned along the azimuthal direction. Meanwhile, since e_r is $\pi/2$ out of phase with respect to e_z, the electric polarization of the mode is elliptical in the meridional rz plane. The full mode functions of TM modes are given by $\boldsymbol{\mathcal{E}}^{(f)} = \mathbf{e}^{(f)}e^{if\beta z}$ and $\boldsymbol{\mathcal{H}}^{(f)} = \mathbf{h}^{(f)}e^{if\beta z}$.

III. SPATIAL INTENSITY DISTRIBUTIONS

In this section, we study the electric intensity distributions $|\mathbf{e}|^2 = |e_r|^2 + |e_\varphi|^2 + |e_z|^2$ of the fields in the fundamental HE_{11} and several higher-order modes, namely the TE_{01}, TM_{01}, HE_{21}, and EH_{11} modes. In the cases of the hybrid HE_{11}, HE_{21}, and EH_{11} modes, we examine both quasicircular and quasilinear polarizations.

The cross-sectional profiles of the electric intensity distributions $|\mathbf{e}|^2$ of the fields in the quasicircularly polarized HE_{11} mode, the TE_{01} mode, the TM_{01} mode, and the quasicircularly polarized HE_{21} mode are shown in Fig. 3. One can note that all of them are azimuthally symmetric. To show the spatial
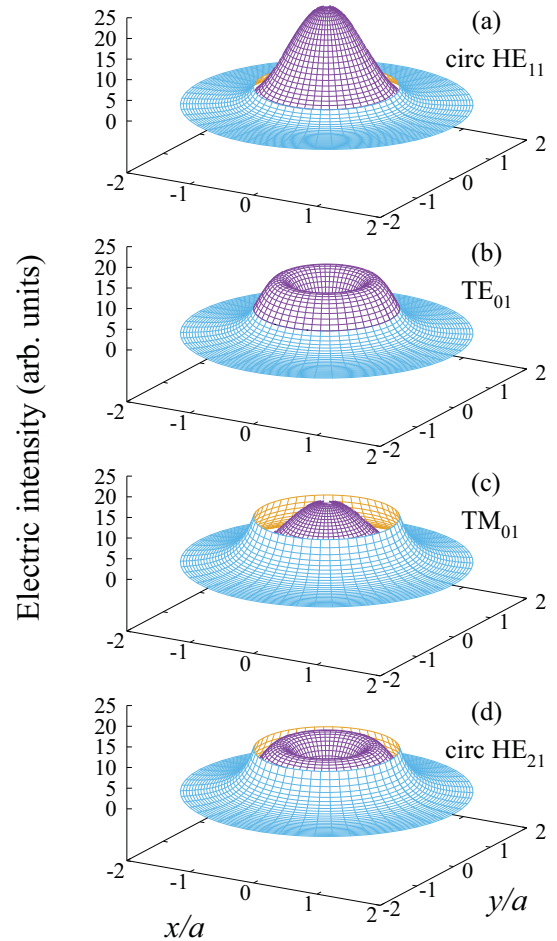
FIG. 3. Cross-sectional profiles of the electric intensity distributions $|\mathbf{e}|^2$ of the fields in (a) the quasicircularly polarized HE_{11} mode, (b) the TE_{01} mode, (c) the TM_{01} mode, and (d) the quasicircularly polarized HE_{21} mode. The inner ($r/a < 1$) and outer ($r/a > 1$) parts are distinguished by the blue (dark gray) and cyan (light gray) colors, respectively. In all four cases, the distributions are normalized to the same power. The fiber radius is chosen to be $a = 400$ nm. All other parameters are as for Fig. 1.
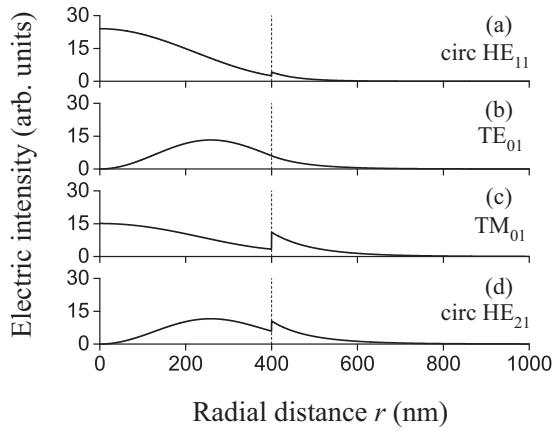
FIG. 4. Electric intensities $|\mathbf{e}|^2$ of the fields in (a) the quasicircularly polarized HE_{11} mode, (b) the TE_{01} mode, (c) the TM_{01} mode, and (d) the quasicircularly polarized HE_{21} mode as functions of the radial distance r. The parameters used are the same as for Fig. 3. The vertical dotted lines indicate the position of the fiber surface.

FIG. 6. Electric intensities $|\mathbf{e}|^2$ of the fields in the quasilinearly polarized (a) HE_{11} and (b) HE_{21} modes as functions of the radial distance r for two different angles φ. The parameters used are as for Fig. 5. The vertical dotted lines indicate the position of the fiber surface.

dependencies of these distributions more clearly, we display in Fig. 4 cuts in the radial direction. We note that the group of the TE_{01}, TM_{01}, and HE_{21} modes corresponds to the first higher-order LP_{11} mode of weakly guiding fibers [41]. Meanwhile, the fundamental HE_{11} mode corresponds to the lowest LP_{01} mode of weakly guiding fibers [41].

For hybrid modes, we can use quasilinear polarization instead of quasicircular polarization. In order to illustrate fields in hybrid modes with quasilinear polarization, we display in Fig. 5 the cross-sectional profiles of the electric intensity distributions $|\mathbf{e}|^2$ of the fields in the quasilinearly polarized HE_{11} and HE_{21} modes. To show the spatial dependencies more clearly, radial cuts for both modes in two different directions are shown in Fig. 6.
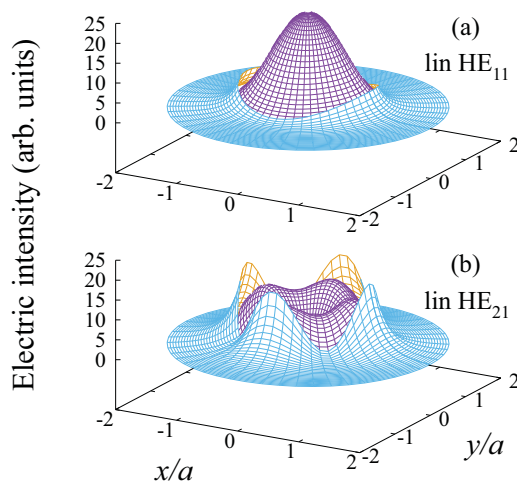
In addition to the TE, TM, and HE modes, there is another type of guided modes, namely the EH modes. The cross-sectional profiles of the electric intensity distributions $|\mathbf{e}|^2$ of the fields in the quasicircularly and quasilinearly polarized EH_{11} modes are shown in Fig. 7. Similarly, Fig. 8 depicts cuts in the radial direction.

Figures 3–8 show that the shapes of the profiles inside and outside the fiber are very different from each other. Inside the fiber, the field intensity is not a fast reducing function of the radial distance r. A discontinuity of the field intensity is observed at the position of the fiber surface. This discontinuity is due to the boundary condition for the normal (radial)

FIG. 5. Cross-sectional profiles of the electric intensity distributions $|\mathbf{e}|^2$ of the fields in the quasilinearly polarized (a) HE_{11} and (b) HE_{21} modes. The inner ($r/a < 1$) and outer ($r/a > 1$) parts are distinguished by the blue (dark gray) and cyan (light gray) colors, respectively. The symmetry axis orientation angle is $\varphi_{\text{pol}} = 0$. Other parameters are as for Figs. 1 and 3.
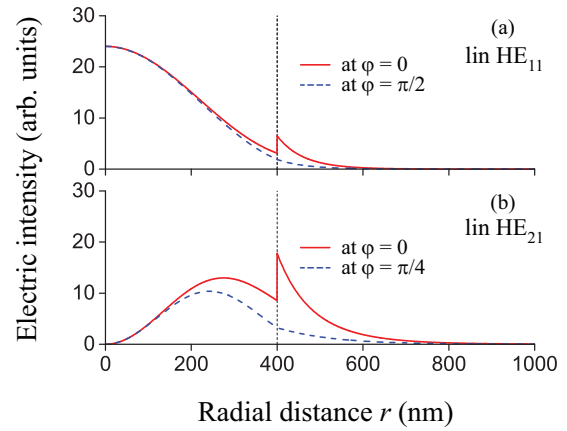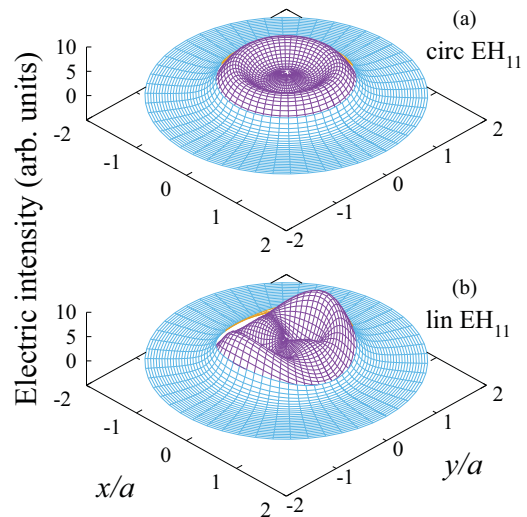

FIG. 7. Cross-sectional profiles of the electric intensity distributions $|\mathbf{e}|^2$ of the fields in (a) the quasicircularly and (b) the quasilinearly polarized EH_{11} modes. The inner ($r/a < 1$) and outer ($r/a > 1$) parts are distinguished by the blue (dark gray) and cyan (light gray) colors, respectively. The fiber radius is $a = 600$ nm. In (b), the symmetry axis orientation angle is $\varphi_{\text{pol}} = 0$. Other parameters are as for Fig. 1.
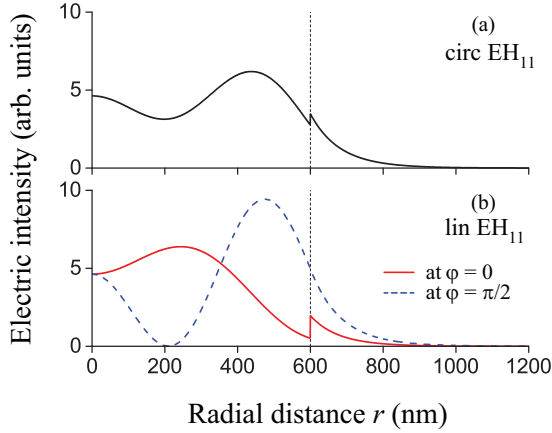
FIG. 8. Electric intensities $|\mathbf{e}|^2$ of the fields in (a) the quasicircularly and (b) the quasilinearly polarized EH_{11} modes as functions of the radial distance r. The parameters used are the same as for Fig. 7. The vertical dotted lines indicate the position of the fiber surface.

FIG. 9. Effective mode radius r_{eff} as a function of the fiber radius a. The parameters used are the same as for Fig. 1.

component e_r of the electric field. Since the difference between the refractive indices of the silica core and the vacuum cladding is large, the discontinuity of the field at the position of the fiber surface is dramatic.

Outside the fiber, the field intensity monotonically and quickly reduces with increasing radial distance r. This behavior is a consequence of the evanescent-wave nature of guided fields, which do not propagate along the radial direction. Comparison between the parts of Fig. 4 shows that, for the parameters used, the fraction of the field intensity distribution outside the fiber for higher-order modes is larger than that for the HE_{11} mode.

We observe from Figs. 3 and 7(a) that, for quasicircularly polarized hybrid HE and EH modes, TE modes, and TM modes, the spatial distribution of the field intensity is cylindrically symmetric. In these cases, the outer parts of the electric intensity distributions of the different modes look very similar to each other as they exhibit the evanescent wave behavior. Meanwhile, the inner parts of the electric intensity distributions of different modes look very different from each other. Indeed, the inner parts of the electric intensity profiles have the shape of a cone in Figs. 3(a) and 3(c), the shape of a doughnut in Figs. 3(b) and 3(d), and the shape of a combination of a cone and a doughnut in Fig. 7(a).

We observe from Figs. 5 and 7(b) that, for quasilinearly polarized hybrid modes, the spatial distribution of the field intensity is not cylindrically symmetric. In the inner and outer vicinities of the fiber surface, the field intensity strongly varies with varying azimuthal angle.

Finally, from Figs. 4(b), 4(d), and 6(b) one can see that, in the cases of the TE_{01} and HE_{21} modes, the electric field intensity is exactly equal to zero at the center of the fiber. Figure 8(b) shows that, for the quasilinearly polarized EH_{11} mode, the electric field intensity is exactly equal to zero at two centrally symmetric off-center positions along the y axis inside the fiber.

The spatial profiles of the fields presented in Figs. 3–6 are in agreement with the results of Refs. [28,36,38], where the spatial profiles were depicted as 2D contour plots. We note that
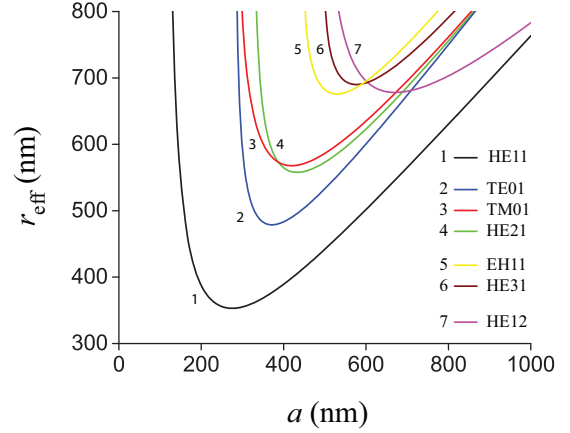
it is not easy to see the accurate magnitude of the intensity and the fine features of the profiles in 2D contour plots. In addition, the cases of hybrid modes with quasicircular polarization were not discussed in Refs. [28,36,38].

The effective mode area can be defined as $A_{\mathrm{eff}} = (\int |\mathbf{e}|^2 d\mathbf{r})^2 / \int |\mathbf{e}|^4 d\mathbf{r}$, where we use the notation $\int d\mathbf{r} = \int_0^{2\pi} d\varphi \int_0^\infty r\, dr$. This allows us to define an effective mode radius as $r_{\mathrm{eff}} = \sqrt{A_{\mathrm{eff}}/\pi}$. The parameters A_{eff} and r_{eff} characterize the confinement of the field mode in the fiber transverse plane. We show in Fig. 9 the effective mode radius r_{eff} as a function of the fiber radius a for the fundamental mode and several higher-order modes. It is clear that the effective radii of the higher-order modes are larger than that of the fundamental mode. In addition, different modes have different minimum effective radii. These minimum values are achieved at different points corresponding to different values of a. For the light wavelength $\lambda = 780$ nm used in our numerical calculations, the smallest value of r_{eff} is about 353 nm and is achieved for the fundamental HE_{11} mode of a fiber with the radius $a = 275$ nm.

IV. POYNTING VECTOR, POWER, AND ENERGY PER UNIT LENGTH

Next, we calculate the Poynting vector, propagating power, and energy per unit length. We show that the axial and azimuthal components of the Poynting vector can be negative with respect to the direction of propagation and the direction of phase circulation, respectively. In order to get deeper insight into the connection between linear and angular momenta of light, we also study the decomposition of the Poynting vector into the orbital and spin parts. We show that the orbital and spin parts of the Poynting vector can have opposite signs in some regions of space.

A. Poynting vector

An important characteristic of light propagation is the cycle-averaged Poynting vector

$$\mathbf{S} = \tfrac{1}{2}\mathrm{Re}(\boldsymbol{\mathcal{E}} \times \boldsymbol{\mathcal{H}}^*). \qquad (12)$$

We introduce the notations S_z, S_φ, and S_r for the axial, azimuthal, and radial components of the vector $\mathbf{S}$ in the
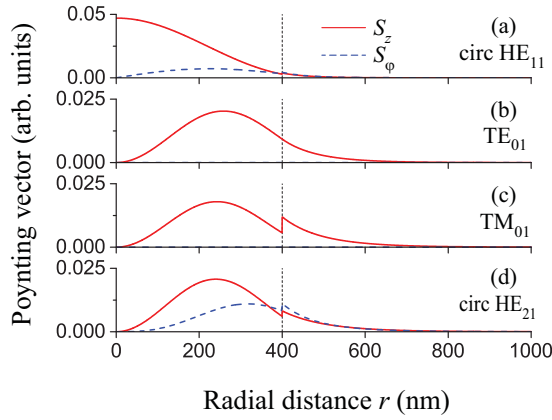
FIG. 10. Components S_z (solid red curves) and S_φ (dashed blue curves) of the Poynting vectors of the fields in (a) the quasicircularly polarized HE_{11} mode, (b) the TE_{01} mode, (c) the TM_{01} mode, and (d) the quasicircularly polarized HE_{21} mode as functions of the radial distance r. The fiber radius is $a = 400$ nm and the same power is used for calculations in all four cases. The propagation direction index is $f = +$ and the phase circulation direction index for the HE modes is $p = +$. All other parameters are as for Fig. 1. The vertical dotted lines indicate the position of the fiber surface.

cylindrical coordinates. For guided modes of fibers, we have $S_r = 0$ and

$$S_z = \tfrac{1}{2}\mathrm{Re}(\mathcal{E}_r \mathcal{H}_\varphi^* - \mathcal{E}_\varphi \mathcal{H}_r^*), \quad S_\varphi = \tfrac{1}{2}\mathrm{Re}(\mathcal{E}_z \mathcal{H}_r^* - \mathcal{E}_r \mathcal{H}_z^*).$$

$$(13)$$

The explicit expressions for S_z and S_φ are given by Eqs. (B1)–(B8) in Appendix B. We note that the existence of a nonzero azimuthal component S_φ of the Poynting vector for guided fields leads to a force transverse to the direction of propagation. This is similar to the situation for light beams with a transverse phase gradient, for which transverse optical forces have been experimentally observed [42].

It is worth nothing that, due to the interference between different terms associated with different Bessel functions, the sign of the azimuthal component S_φ of the Poynting vector of a quasicircularly polarized hybrid mode and the sign of the axial component S_z of the Poynting vector of a quasilinearly polarized hybrid mode can vary in space. The details are given in Appendix B.

For the quasicircularly polarized HE_{11} mode, the TE_{01} mode, the TM_{01} mode, and the quasicircularly polarized HE_{21} mode, the axial component S_z and the azimuthal component S_φ of the Poynting vector are shown in Fig. 10. The dashed blue curves in Figs. 10(a) and 10(d) show that the azimuthal component S_φ is nonzero for the quasicircularly polarized hybrid modes. In these cases, outside the fiber, the azimuthal component S_φ is comparable to [see Fig. 10(a)] and may even be slightly larger than [see Fig. 10(d)] the axial component S_z. For the parameters used, both components S_z and S_φ are positive. According to Figs. 10(b) and 10(c) and Appendix B, the azimuthal component S_φ of the Poynting vector is vanishing for TE and TM modes. The figure indicates that the fractional power outside the fiber for higher-order modes is larger than that for the fundamental HE_{11} mode.
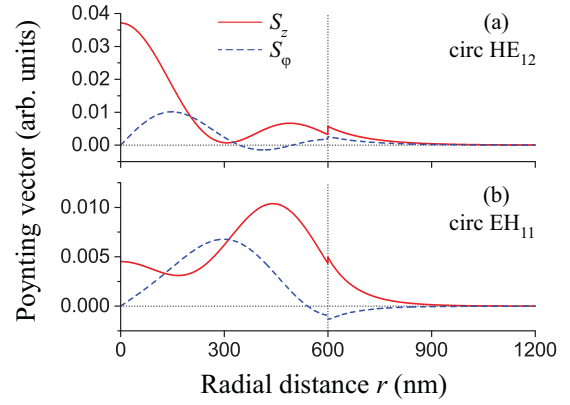

FIG. 11. Components S_z (solid red curves) and S_φ (dashed blue curves) of the Poynting vectors of the fields in the quasicircularly polarized (a) HE_{12} and (b) EH_{11} modes as functions of the radial distance r. The fiber radius is $a = 600$ nm and all other parameters are as for Figs. 1 and 10. The vertical dotted lines indicate the position of the fiber surface.

The axial component S_z and the azimuthal component S_φ of the Poynting vector for the quasicircularly polarized HE_{12} and EH_{11} modes are displayed in Fig. 11. The dashed blue curves of the figure show that S_φ is negative in a localized region of space. For the HE_{12} mode [Fig. 11(a)], this region is inside the fiber. However, for the EH_{11} mode [Fig. 11(b)], part of this region is the outside and part is in the inside of the fiber.

Figures 10(a), 10(d), 11(a), and 11(b) and additional numerical calculations, which are not shown here, confirm that, outside the fiber, the azimuthal component S_φ of the Poynting vector is positive for quasicircularly polarized HE modes but negative for quasicircularly polarized EH modes.

It is not surprising that a component of the Poynting vector can have different signs in different regions of space [43,44]. Similar results have been obtained for the axial component of the Poynting vector of a guided mode [43] and for the axial and azimuthal components of the Poynting vector of a Bessel beam [44]. In fact, we have confirmed that the axial component S_z of the Poynting vector of the quasilinearly polarized HE_{11} mode can become negative when the refractive index n_1 of the fiber is large enough ($n_1/n_2 > 2.71$ for the HE_{11} mode) [43]. We show in Fig. 12 a similar result for the quasilinearly polarized higher-order HE_{21} mode. One can see that in this case the Poynting vector is negative in four regions around the fiber surface at azimuthal angles around the values $\varphi = 0$, $\pi/2$, π, and $3\pi/2$.

B. Propagating power

The optical power carried by the fiber is given by

$$P = \int S_z \, d\mathbf{r}. \qquad (14)$$

It can be split as $P = P_{\mathrm{in}} + P_{\mathrm{out}}$, where P_{in} and P_{out} are the propagating powers inside and outside the fiber and explicit expressions for both are given by Eqs. (C1)–(C6) in Appendix C.

The fractional power outside the fiber η_P is defined as $\eta_P = P_{\mathrm{out}}/P$. We display η_P in Fig. 13 as a function of the fiber
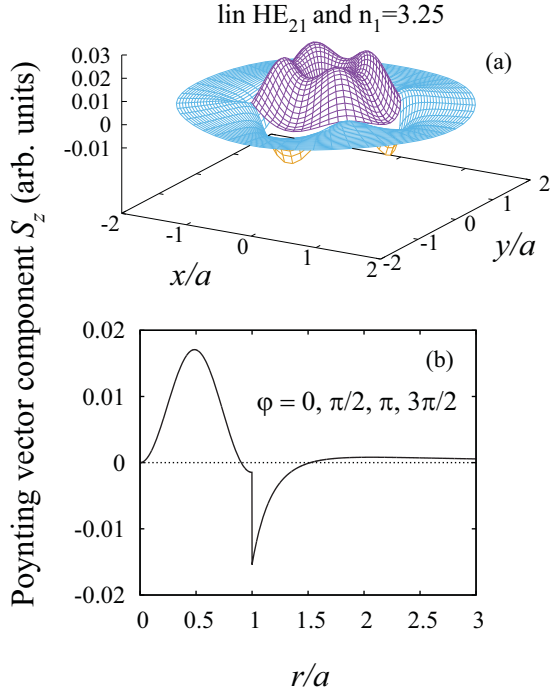
FIG. 12. (a) Cross-sectional profile and (b) radial dependence of the axial Poynting vector component S_z of the quasilinearly polarized HE_{21} mode. The refractive indices of the fiber and the surrounding medium are $n_1 = 3.25$ and $n_2 = 1$. The fiber radius is $a = 270$ nm and the wavelength of light is $\lambda = 1500$ nm.

radius a for the HE_{11} mode and several higher-order modes. We observe from the figure that η_P reduces with increasing a and that the fractional powers outside the fiber for higher-order modes are larger than that for the fundamental mode. It is interesting to note that, near the cutoffs for the EH_{11} and HE_{31} modes, the factor η_P is significantly smaller than unity, unlike the cases of the HE_{11} and HE_{12} modes. We show in Appendix C that, for the EH_{lm} modes with $l = 1, 2, \ldots$ and the HE_{lm} modes with $l = 3, 4, \ldots$, the limiting values of the factor

η_P in the cutoff regions are smaller than unity, in agreement with the aforementioned numerical results. We also show in Appendix C that, for the TE_{0m} and TM_{0m} modes and the HE_{lm} modes with $l = 1$ or 2, the limiting values of the factor η_P in the cutoff regions are equal to unity. Despite this prediction, we observe from Fig. 13 that, in the vicinities of the cutoffs, the factors η_P for the TE_{01}, TM_{01}, and HE_{21} modes are slightly smaller than unity. These numerical deviations are due to the steep slopes of the curves that make it difficult to approach the cutoffs. Note that the numerical results presented in Fig. 13 are in agreement with the results presented in Ref. [45], where the fractional power outside the fiber was calculated for a few modes and was plotted as a function of the fiber size parameter. We emphasize again that the fiber size parameter is not a rigorous scaling parameter since the fiber material is dispersive. In addition, the limiting values of the fractional power outside the fiber near the cutoffs were not discussed in Ref. [45].

C. Energy per unit length

The cycle-averaged energy per unit length is given by

$$U = \frac{\epsilon_0}{4} \int n^2 |\mathcal{E}|^2 \, d\mathbf{r} + \frac{\mu_0}{4} \int |\mathcal{H}|^2 \, d\mathbf{r}, \quad (15)$$

where $n(r) = n_1$ for $r < a$ and n_2 for $r > a$. The first and second terms on the right-hand side of expression (15) correspond to the electric and magnetic parts, respectively, of the energy of the field. For guided modes, these parts are equal to each other. We can split U as $U = U_{in} + U_{out}$, where U_{in} and U_{out} are the energies per unit length inside and outside the fiber, and their explicit expressions are given by Eqs. (D1)–(D6) in Appendix D.

The fractional energy outside the fiber $\eta_U = U_{out}/U$ is shown as a function of the fiber radius a for the HE_{11} mode and several higher-order modes in Fig. 14. One can see that the behavior of η_U is very similar, but not identical, to that of η_P.

FIG. 13. Fractional power outside the fiber η_P as a function of the fiber radius a. The parameters used are as for Fig. 1. The vertical dotted lines indicate the positions of the cutoffs for higher-order modes.
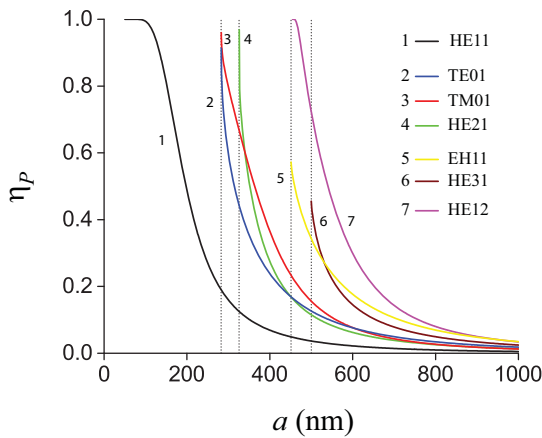

FIG. 14. Fractional energy outside the fiber η_U as a function of the fiber radius a. The parameters used are as for Fig. 1. The vertical dotted lines indicate the positions of the cutoffs for higher-order modes.
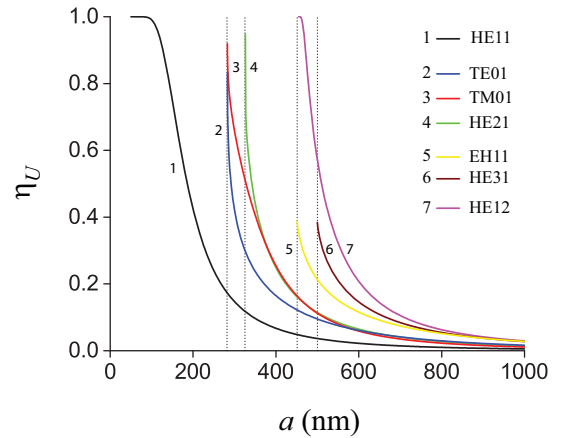
D. Orbital and spin parts of the Poynting vector

It is known that the Poynting vector of the field can be decomposed into two parts, the orbital part and the spin part [46–52]. In the dual-symmetric formalism, the decomposition takes the form [46–52]

$$\mathbf{S} = \mathbf{S}^{\text{orb}} + \mathbf{S}^{\text{spin}}, \tag{16}$$

where $\mathbf{S}^{\text{orb}} = \mathbf{S}^{\text{e-orb}} + \mathbf{S}^{\text{h-orb}}$ is the orbital part, with its electric and magnetic components

$$\mathbf{S}^{\text{e-orb}} = \frac{c\epsilon_0}{4k}\text{Im}[\boldsymbol{\mathcal{E}}^* \cdot (\boldsymbol{\nabla})\boldsymbol{\mathcal{E}}],$$
$$\mathbf{S}^{\text{h-orb}} = \frac{c\mu_0}{4kn^2}\text{Im}[\boldsymbol{\mathcal{H}}^* \cdot (\boldsymbol{\nabla})\boldsymbol{\mathcal{H}}], \tag{17}$$

and $\mathbf{S}^{\text{spin}} = \mathbf{S}^{\text{e-spin}} + \mathbf{S}^{\text{h-spin}}$ is the spin part, with its electric and magnetic components

$$\mathbf{S}^{\text{e-spin}} = \frac{c\epsilon_0}{8k}\boldsymbol{\nabla} \times \text{Im}(\boldsymbol{\mathcal{E}}^* \times \boldsymbol{\mathcal{E}}),$$
$$\mathbf{S}^{\text{h-spin}} = \frac{c\mu_0}{8kn^2}\boldsymbol{\nabla} \times \text{Im}(\boldsymbol{\mathcal{H}}^* \times \boldsymbol{\mathcal{H}}). \tag{18}$$

In Eq. (17), the dot product applies to the field vectors, that is, $\boldsymbol{\mathcal{A}} \cdot (\boldsymbol{\nabla})\boldsymbol{\mathcal{B}} \equiv \sum_{i=x,y,z} \mathcal{A}_i \boldsymbol{\nabla} \mathcal{B}_i$ for arbitrary field vectors $\boldsymbol{\mathcal{A}}$ and $\boldsymbol{\mathcal{B}}$.

In general, we have the equality $\mathbf{S}^{\text{e}} = \mathbf{S}^{\text{h}}$, where $\mathbf{S}^{\text{e}} = \mathbf{S}^{\text{e-orb}} + \mathbf{S}^{\text{e-spin}}$ and $\mathbf{S}^{\text{h}} = \mathbf{S}^{\text{h-orb}} + \mathbf{S}^{\text{h-spin}}$ are the electric and magnetic components of the Poynting vector. However, we may observe the inequalities $\mathbf{S}^{\text{e-orb}} \neq \mathbf{S}^{\text{h-orb}}$ and $\mathbf{S}^{\text{e-spin}} \neq \mathbf{S}^{\text{h-spin}}$. The explicit expressions for the electric and magnetic components of the orbital and spin parts of the Poynting vector of guided light are given in Appendix E. It is worth noting that the orbital part $\mathbf{S}^{\text{orb}}$ of the Poynting vector is proportional to the canonical momentum of light, which determines the radiation pressure force upon a small dipole Rayleigh particle [48–52].

We show in Appendix E that the orbital parts S_z^{orb} and S_φ^{orb} of the axial and azimuthal components, respectively, of the Poynting vector are positive with respect to the direction of propagation and the direction of phase circulation, respectively. Meanwhile, the signs of the spin parts, S_z^{spin} and S_φ^{spin}, of the Poynting vector can vary in the fiber transverse plane and can hence be negative with respect to the direction of propagation and the direction of phase circulation, respectively, in some regions of space. Thus, the orbital and spin parts of the Poynting vector can have opposite signs in certain regions of space. We show numerical results confirming this in Figs. 15–17.

We show in Appendix E that the orbital part S_z^{orb} of the axial component S_z of the Poynting vector is determined by the local density of energy. Meanwhile, the orbital part S_φ^{orb} of the azimuthal component S_φ of the Poynting vector of a quasicircularly polarized hybrid mode depends on not only the local phase gradient but also the local polarization, unlike the case of uniformly polarized paraxial beams [52].

The radial dependencies of the orbital part S_z^{orb} and the spin part S_z^{spin} of the axial component S_z of the Poynting vector for the quasicircularly polarized HE_{11} mode, the TE_{01} mode, the TM_{01} mode, and the quasicircularly polarized HE_{21} mode are shown in Fig. 15. The radial dependencies of the orbital part S_φ^{orb} and the spin part S_φ^{spin} of the azimuthal component
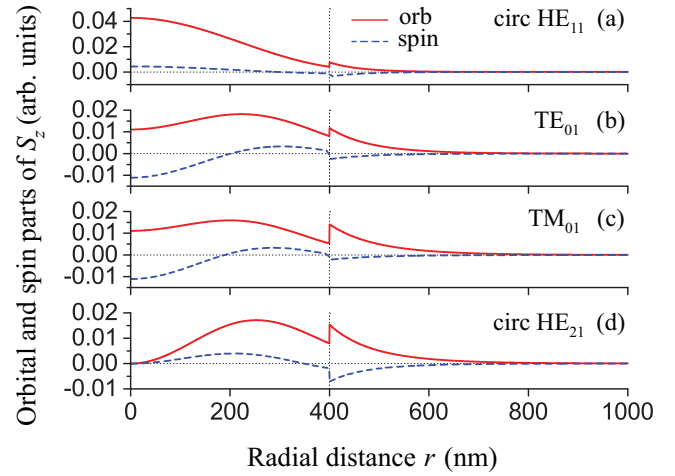

FIG. 15. Orbital part S_z^{orb} (solid red curves) and spin part S_z^{spin} (dashed blue curves) of the axial component S_z of the Poynting vector as functions of the radial distance r. The field is in (a) the quasicircularly polarized HE_{11} mode, (b) the TE_{01} mode, (c) the TM_{01} mode, and (d) the quasicircularly polarized HE_{21} mode. The fiber radius is $a = 400$ nm and the same power is used for calculations in all four cases. The propagation direction index is $f = +$ and the phase circulation direction index for the HE modes in parts (a) and (d) is $p = +$. All other parameters are as for Fig. 1. The vertical dotted lines indicate the position of the fiber surface.

S_φ of the Poynting vector for the quasicircularly polarized HE_{11} and HE_{21} modes are shown in Fig. 16. Additionally, the radial dependencies of the orbital and spin parts of the axial and azimuthal components of the Poynting vector for the quasicircularly polarized EH_{11} mode are displayed in Fig. 17.
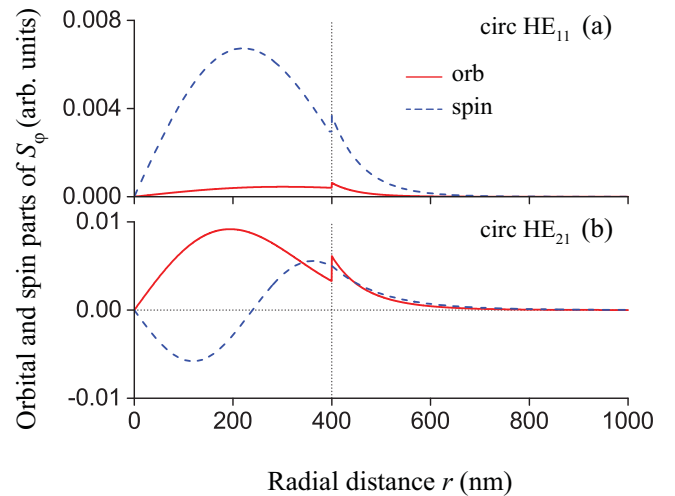
FIG. 16. Orbital part S_φ^{orb} (solid red curves) and spin part S_φ^{spin} (dashed blue curves) of the azimuthal component S_φ of the Poynting vector as functions of the radial distance r. The field is in the quasicircularly polarized (a) HE_{11} and (b) HE_{21} modes. The fiber radius is $a = 400$ nm and the same power is used for calculations in both cases. The propagation direction index is $f = +$ and the phase circulation direction index is $p = +$. All other parameters are as for Fig. 1. The vertical dotted lines indicate the position of the fiber surface.
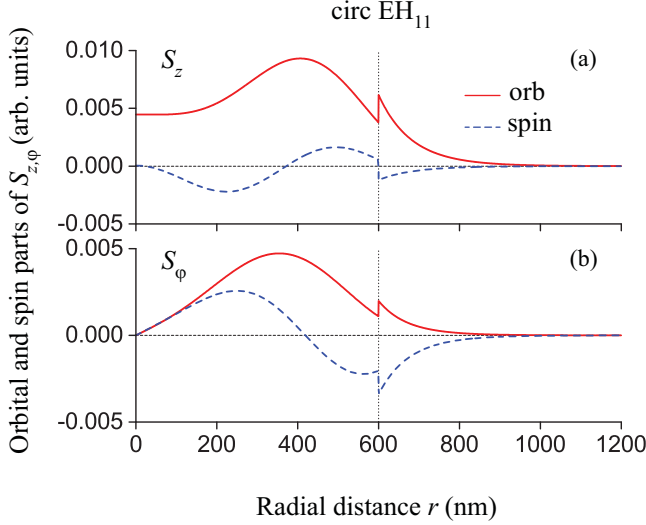
FIG. 17. Orbital (solid red curves) and spin (dashed blue curves) of (a) the axial component and (b) the azimuthal component of the Poynting vector of the quasicircularly polarized EH_{11} mode as functions of the radial distance r. The fiber radius is $a = 600$ nm. The propagation direction index is $f = +$ and the phase circulation direction index is $p = +$. All other parameters are as for Fig. 1. The vertical dotted lines indicate the position of the fiber surface.

These figures show that the orbital parts S_z^{orb} and S_φ^{orb} of the axial and azimuthal components of the Poynting vector are positive with respect to the direction of propagation and the direction of phase circulation, respectively. However, the signs of the spin parts S_z^{spin} and S_φ^{spin} of the axial and azimuthal components can vary inside the fiber. We observe from Figs. 15 and 17(a) that, outside the fiber, the spin part S_z^{spin} of the axial component S_z of the Poynting vector is negative. Figures 16 and 17(b) show that, outside the fiber, the spin part S_φ^{spin} of the azimuthal component S_φ of the Poynting vector is positive for HE modes and is negative for EH modes. These features are also observed for S_φ (see Figs. 10 and 11).

V. ANGULAR MOMENTUM OF GUIDED LIGHT

In this section, we calculate the angular momentum of guided light and also study its orbital, spin, and surface parts. We show that the orbital part of angular momentum depends not only on the phase gradient, but also on the field polarization, and is always positive with respect to the direction of the phase circulation axis. Meanwhile, the spin and surface parts of angular momentum and the helicity (chirality) of light can be negative with respect to the direction of the phase circulation axis. We find that the signs of the spin and surface parts of the transverse angular momentum density of the fundamental and higher-order modes depend on the direction of propagation.

A. Angular momentum of guided light

For the electromagnetic field in free space, the linear momentum density is given by $\mathbf{p}_{local} = \mathbf{S}/c^2$ [53]. For the field in a dielectric medium, several formulations for the linear momentum density can be found in the literature [54]. The

Abraham formulation [55] takes $\mathbf{p}_{local} = [\mathbf{E} \times \mathbf{H}]/c^2$, which is sometimes interpreted as the field-only contribution to the momentum of light. On the other hand, the Minkowski formulation [56] takes $\mathbf{p}_{local} = [\mathbf{D} \times \mathbf{B}]$. While the appropriate form remains contentious because the debate has not been settled by experiments, the Abraham formulation is generally accepted [53,57]. Therefore, in our basic calculations, we adopt the Abraham formulation for the field linear momentum density inside and outside the fiber.

With the above definition of the linear momentum density, the angular momentum density of the electromagnetic field is given by $\mathbf{j}_{local} \equiv (\mathbf{R} \times \mathbf{p}_{local}) = (\mathbf{R} \times \mathbf{S})/c^2$. Here, $\mathbf{R} = x\hat{\mathbf{x}} + y\hat{\mathbf{y}} + z\hat{\mathbf{z}}$ is the position vector in the three-dimensional space. Integrating $\mathbf{j}_{local}$ over the cross-sectional plane of the fiber then yields the angular momentum per unit length

$$\mathbf{J} \equiv \int \mathbf{j}_{local} \, d\mathbf{r} = \frac{1}{c^2} \int (\mathbf{R} \times \mathbf{S}) \, d\mathbf{r}. \tag{19}$$

Note that TE and TM modes and quasilinearly polarized HE and EH modes have no angular momentum.

We consider the cycle-averaged angular momentum per unit length $\mathbf{J}$ of quasicircularly polarized HE and EH modes. The only nonzero component of $\mathbf{J}$ is aligned along the fiber axis and is given by

$$J_z = \frac{1}{c^2} \int r S_\varphi \, d\mathbf{r}. \tag{20}$$

Thus, the axial angular momentum per unit length J_z is determined by the azimuthal component S_φ of the Poynting vector. We can write $J_z = J_z^{in} + J_z^{out}$, where J_z^{in} and J_z^{out} are the parts of the angular momentum of light inside and outside the fiber. The explicit analytical expressions for J_z^{in} and J_z^{out} are given by Eqs. (F1) and (F2) in Appendix F. According to these expressions, the axial angular momentum per unit length J_z depends on the direction of phase circulation, specified by the index p, but does not depend on the direction of propagation, specified by the index f.

The angular momentum per photon $j_z = \hbar\omega J_z/U$ for quasicircularly polarized hybrid modes with the positive (counterclockwise) phase circulation direction $p = +$ is shown as a function of the fiber radius a in Fig. 18. One can see that j_z decreases with increasing a and increases with increasing l. Comparison between HE and EH modes shows that, for a given set of l and m, the angular momentum per photon j_z for an EH_{lm} mode is smaller than that for the corresponding HE_{lm} mode. This feature is related to the fact that, outside the fiber, the azimuthal component S_φ of the Poynting vector is positive for HE modes and is negative for EH modes (see Fig. 11). Figure 18 also shows that the EH_{11} mode has the lowest angular momentum per photon. It is clear that the angular momentum per photon in a higher-order hybrid mode is large when the azimuthal mode order l is large.

B. Orbital and spin parts of angular momentum

The angular momentum per unit length $\mathbf{J}$ of a light beam can be decomposed into orbital, spin, and surface parts as $\mathbf{J} = \mathbf{J}^{orb} + \mathbf{J}^{spin} + \mathbf{J}^{surf}$ [58–62]. However, the identification of terms as orbital, spin, and surface components is not unique [63,64].
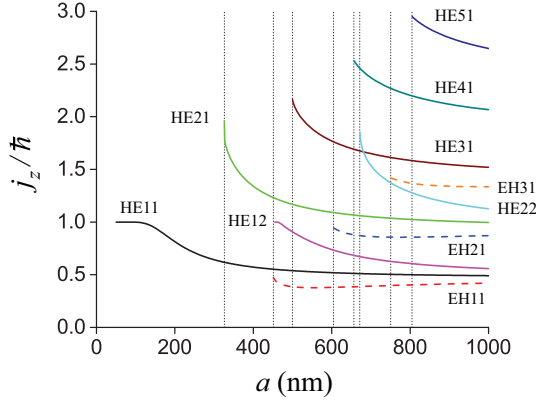
FIG. 18. Angular momentum per photon j_z as a function of the fiber radius a for quasicircularly polarized hybrid modes with the positive phase circulation direction $p = +$. The parameters used are as for Fig. 1. The vertical dotted lines indicate the positions of the cutoffs for higher-order modes.

In the dual-symmetric formalism, the orbital and spin parts of angular momentum per unit length are given as [49–52,65]

$$\mathbf{J}^{\text{orb}} = \frac{\epsilon_0}{4\omega} \int \text{Im}[\boldsymbol{\mathcal{E}}^* \cdot (\mathbf{R} \times \nabla)\boldsymbol{\mathcal{E}}]\, d\mathbf{r}$$
$$+ \frac{\mu_0}{4\omega} \int \frac{1}{n^2} \text{Im}[\boldsymbol{\mathcal{H}}^* \cdot (\mathbf{R} \times \nabla)\boldsymbol{\mathcal{H}}]\, d\mathbf{r} \quad (21)$$

and

$$\mathbf{J}^{\text{spin}} = \frac{\epsilon_0}{4\omega} \int \text{Im}(\boldsymbol{\mathcal{E}}^* \times \boldsymbol{\mathcal{E}})\, d\mathbf{r} + \frac{\mu_0}{4\omega} \int \frac{1}{n^2} \text{Im}(\boldsymbol{\mathcal{H}}^* \times \boldsymbol{\mathcal{H}})\, d\mathbf{r}.$$
$$(22)$$

In Eq. (21), the dot product applies to the field vectors, that is, $\boldsymbol{\mathcal{A}} \cdot (\mathbf{R} \times \nabla)\boldsymbol{\mathcal{B}} \equiv \sum_{i=x,y,z} \mathcal{A}_i(\mathbf{R} \times \nabla)\mathcal{B}_i$ for arbitrary field vectors $\boldsymbol{\mathcal{A}}$ and $\boldsymbol{\mathcal{B}}$. Detailed discussions of various aspects of optical orbital angular momentum can be found in Ref. [66].

Meanwhile, the surface part of angular momentum per unit length is, in the dual-symmetric formalism, given as [58–62]

$$\mathbf{J}^{\text{surf}} = -\frac{\epsilon_0}{4\omega} \int \text{Im}[\nabla \cdot \boldsymbol{\mathcal{E}}^*(\mathbf{R} \times \boldsymbol{\mathcal{E}})]\, d\mathbf{r}$$
$$- \frac{\mu_0}{4\omega} \int \frac{1}{n^2} \text{Im}[\nabla \cdot \boldsymbol{\mathcal{H}}^*(\mathbf{R} \times \boldsymbol{\mathcal{H}})]\, d\mathbf{r}, \quad (23)$$

where we have used the notation $\nabla \cdot \boldsymbol{\mathcal{A}}(\mathbf{R} \times \boldsymbol{\mathcal{B}}) = \sum_{i=x,y,z} \nabla_i[\mathcal{A}_i(\mathbf{R} \times \boldsymbol{\mathcal{B}})]$.

The orbital part of angular momentum per unit length is related to the orbital part $\mathbf{S}^{\text{orb}}$ of the Poynting vector via the formula $\mathbf{J}^{\text{orb}} = (1/c^2) \int (\mathbf{R} \times \mathbf{S}^{\text{orb}})\, d\mathbf{r}$. The spin and surface parts of angular momentum per unit length are related to the spin part $\mathbf{S}^{\text{spin}}$ of the Poynting vector via the formula $\mathbf{J}^{\text{spin}} + \mathbf{J}^{\text{surf}} = (1/c^2) \int (\mathbf{R} \times \mathbf{S}^{\text{spin}})\, d\mathbf{r}$.

The surface part of angular momentum is usually omitted in the literature [62]. The reason is that, when the field vanishes sufficiently quickly in the limit of large distances, the surface part is, due to the Gaussian theorem, identical to zero. For example, for a bulletlike light wave packet with a finite transverse and longitudinal extent, the surface part of angular momentum can be neglected. However, for a pencil-like light

beam whose span along the direction of propagation is virtually infinite, the surface part is not vanishing [62].

For TE and TM modes, we have $\mathbf{J}^{\text{orb}} = \mathbf{J}^{\text{spin}} = \mathbf{J}^{\text{surf}} = 0$. For quasicircularly polarized HE and EH modes, the only nonzero components of the vectors $\mathbf{J}^{\text{orb}}$, $\mathbf{J}^{\text{spin}}$, and $\mathbf{J}^{\text{surf}}$ are the axial components

$$J_z^{\text{orb}} = p \frac{\epsilon_0}{4\omega} \int [l|\mathbf{e}|^2 - 2\text{Im}(e_r^* e_\varphi)]\, d\mathbf{r}$$
$$+ p \frac{\mu_0}{4\omega} \int \frac{1}{n^2} [l|\mathbf{h}|^2 - 2\text{Im}(h_r^* h_\varphi)]\, d\mathbf{r}, \quad (24)$$

$$J_z^{\text{spin}} = p \frac{\epsilon_0}{2\omega} \int \text{Im}(e_r^* e_\varphi)\, d\mathbf{r} + p \frac{\mu_0}{2\omega} \int \frac{1}{n^2} \text{Im}(h_r^* h_\varphi)\, d\mathbf{r},$$
$$(25)$$

and

$$J_z^{\text{surf}} = p \frac{\pi a^2 \epsilon_0}{2\omega} \text{Im}(e_r^* e_\varphi|_{r=a+0} - e_r^* e_\varphi|_{r=a-0})$$
$$+ p \frac{\pi a^2 \mu_0}{2\omega} \left(\frac{1}{n_2^2} - \frac{1}{n_1^2}\right) \text{Im}(h_r^* h_\varphi)|_{r=a}. \quad (26)$$

Here, we have introduced the notations $a \pm 0 = \lim_{\varepsilon \to 0}(a \pm \varepsilon)$. According to Eqs. (24)–(26), the orbital, spin, and surface parts of the axial angular momentum per unit length J_z depend on the direction of phase circulation p, but not on the direction of propagation f. Equations (24)–(26) are in agreement with the relations $J_z^{\text{orb}} = (1/c^2) \int r S_\varphi^{\text{orb}}\, d\mathbf{r}$ and $J_z^{\text{spin}} + J_z^{\text{surf}} = (1/c^2) \int r S_\varphi^{\text{spin}}\, d\mathbf{r}$.

An important point to note here is that the above results, derived for angular momentum of light in guided modes, are different from the results for angular momentum of light in scalar Laguerre-Gaussian beams [67,68]. The main reason is that a guided light beam is a vector beam [69], whose polarization is not uniform in the cross-sectional plane. Another important reason is that the guided mode has two parts: one inside the fiber, where the medium is a dielectric, and the other one outside the fiber, where the medium is the vacuum. In addition, the discontinuity of the refractive index at the fiber surface leads to the appearance of the surface part of the angular momentum of light.

It follows from Eq. (24) that the orbital part J_z^{orb} of angular momentum of light in an arbitrary hybrid mode is positive or negative when the phase circulation direction index p is positive or negative, respectively. Note that $p = +$ or $-$ means that the phase circulation direction in the xy plane is counterclockwise or clockwise, that is, the phase circulation axis is $+\hat{\mathbf{z}}$ or $-\hat{\mathbf{z}}$, respectively. Thus, the orbital part J_z^{orb} of angular momentum of light in a hybrid mode is positive with respect to the direction of the phase circulation axis. Meanwhile, the expression on the right-hand side of Eq. (24) contains not only the terms $l|\mathbf{e}|^2$ and $l|\mathbf{h}|^2$, which result from the local phase gradient, but also the terms $\text{Im}(e_r^* e_\varphi)$ and $\text{Im}(h_r^* h_\varphi)$, which result from the local polarization. Thus, the orbital part J_z^{orb} of angular momentum depends not only on the phase gradient but also on the field polarization.

Equation (25) shows that the spin part J_z^{spin} of angular momentum is determined by the polarization of the field, whereas, according to Eq. (26), the surface part J_z^{surf} of angular
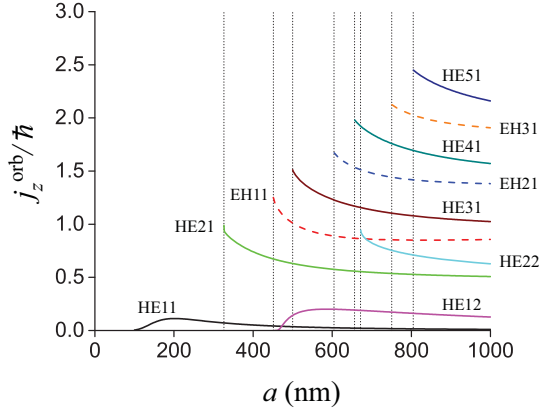
FIG. 19. Orbital angular momentum per photon j_z^{orb} as a function of the fiber radius a for quasicircularly polarized hybrid modes with the positive phase circulation direction $p = +$. The parameters used are as for Fig. 1. The vertical dotted lines indicate the positions of the cutoffs for higher-order modes.

FIG. 20. Spin angular momentum per photon j_z^{spin} as a function of the fiber radius a for quasicircularly polarized hybrid modes with the positive phase circulation direction $p = +$. The parameters used are the same as for Fig. 1. The vertical dotted lines indicate the positions of the cutoffs for higher-order modes. The horizontal dotted line separates the positive and negative sides of the vertical axis.

momentum is associated with the discontinuity of the spin density at the fiber surface. It is clear that the discontinuity of the spin density is induced by the discontinuity of the refractive index of the medium at the fiber surface. Unlike the orbital part J_z^{orb} of angular momentum, both the spin part J_z^{spin} and the surface part J_z^{surf} can be negative with respect to the direction of the phase circulation axis. It is interesting to note that the sum $J_z^{\mathrm{orb}} + J_z^{\mathrm{spin}}$ of the orbital and spin parts is always positive with respect to the direction of the phase circulation axis and is determined by the phase gradient.

We can write $J_z^{\mathrm{orb}} = J_z^{\mathrm{e\text{-}orb}} + J_z^{\mathrm{h\text{-}orb}}$, $J_z^{\mathrm{spin}} = J_z^{\mathrm{e\text{-}spin}} + J_z^{\mathrm{h\text{-}spin}}$, and $J_z^{\mathrm{surf}} = J_z^{\mathrm{e\text{-}surf}} + J_z^{\mathrm{h\text{-}surf}}$. Here, the terms with the letters e and h in the superscripts correspond to the first and second terms, respectively, in Eqs. (24)–(26), and are called the electric and magnetic components, respectively. The explicit analytical expressions for these components are given by Eqs. (F3)–(F8) in Appendix F.

We now introduce the notations $j_z^{\mathrm{orb}} = \hbar\omega J_z^{\mathrm{orb}}/U$, $j_z^{\mathrm{spin}} = \hbar\omega J_z^{\mathrm{spin}}/U$, and $j_z^{\mathrm{surf}} = \hbar\omega J_z^{\mathrm{surf}}/U$ for the orbital, spin, and surface parts of the angular momentum per photon $j_z = \hbar\omega J_z/U$. We show the dependencies of these quantities on the fiber radius a in Figs. 19–21.

One can see from Fig. 19 that the orbital part j_z^{orb} of angular momentum per photon is always positive with respect to the direction of the phase circulation axis, which is in agreement with Eq. (24). Note that j_z^{orb} increases with increasing azimuthal mode order l. It is substantially smaller than $\hbar$ in the cases of the HE_{11} and HE_{12} modes but is comparable to or larger than $\hbar$ in the cases of higher-order HE and EH modes.

From Fig. 20 one can see that the spin part j_z^{spin} of angular momentum per photon is positive with respect to the direction of the phase circulation axis for the HE modes and negative for the EH modes. Furthermore, for the HE_{lm} modes with the azimuthal mode order $l = 1$, the spin part j_z^{spin} is dominant to the orbital part j_z^{orb}. However, for the HE_{lm} modes with $l \geqslant 2$ and the EH_{lm} modes, the orbital part j_z^{orb} is dominant to the spin part j_z^{spin}.

From Fig. 21 one can see that, like the spin part j_z^{spin}, the surface part j_z^{surf} is positive with respect to the direction of the phase circulation axis for the HE modes and negative for the EH modes. Furthermore, the surface part j_z^{surf} is always smaller than $\hbar$. Comparison between Figs. 19–21 shows that, for the HE_{lm} modes with $l = 1$, the surface part j_z^{surf} is substantially smaller than the spin part j_z^{spin} but is comparable to the orbital part j_z^{orb}. For the HE_{lm} modes with $l \geqslant 2$ and the EH modes, the surface part j_z^{surf} is smaller than both the spin part j_z^{spin} and the orbital part j_z^{orb}. Figure 21 and additional calculations indicate that, when the fiber radius a is increased, the surface part j_z^{surf} of angular momentum per photon reduces to zero.

We note that, in the previous work on angular momentum of the fundamental guided mode [70], the orbital angular momentum was defined as $\mathbf{J}^{\mathrm{orb}} = \mathbf{J} - \mathbf{J}^{\mathrm{spin}}$, that is, the surface
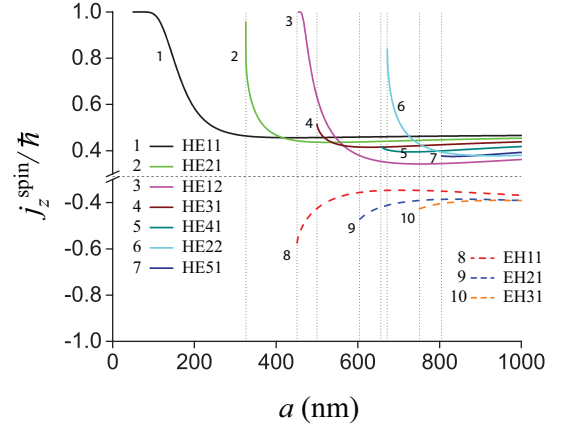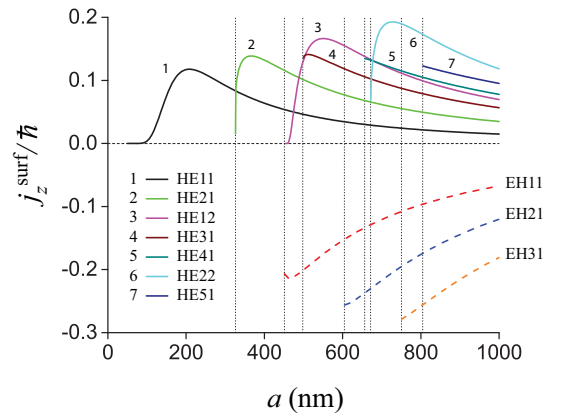

FIG. 21. Surface angular momentum per photon j_z^{surf} as a function of the fiber radius a for quasicircularly polarized hybrid modes with the positive phase circulation direction $p = +$. The parameters used are as for Fig. 1. The vertical dotted lines indicate the positions of the cutoffs for higher-order modes.

angular momentum was included in the orbital angular momentum. In addition, in Ref. [70], the standard electric-bias formalism was used instead of the dual-symmetric formalism. Due to the use of different definitions and different formalisms, the electric spin angular momentum $J_z^{\text{e-spin}}$ in the present work is half of the spin angular momentum J_{spin} in Ref. [70], and the sum of the electric orbital part $J_z^{\text{e-orb}}$ and the electric surface part $J_z^{\text{e-surf}}$ in the present work is half of the orbital angular momentum J_{orb} in Ref. [70].

It is worth noting that the negative sign of the integral spin and surface angular momenta with respect to the direction of the phase circulation axis for the EH modes indicates that their local values are negative in some regions of space. This feature is a consequence of the fact that the spin part of the azimuthal component S_φ of the Poynting vector, which determines the local densities of J_z^{spin} and J_z^{surf} via the relation $J_z^{\text{spin}} + J_z^{\text{surf}} = (1/c^2) \int r S_\varphi^{\text{spin}} d\mathbf{r}$, can be negative [see the dashed blue curves in Figs. 16(b) and 17(b)]. The above result is in agreement with the results of Ref. [68], where it has been shown for Laguerre-Gaussian beams that the local spin density can be positive in some regions and negative in others.

Although the transverse component of angular momentum of guided light is zero, the local density of this component is not zero. Indeed, the local density of the azimuthal component of angular momentum is given by $\rho_{J_\varphi} = -r S_z / c^2$. It can be decomposed as $\rho_{J_\varphi} = \rho_{J_\varphi^{\text{orb}}} + \rho_{J_\varphi^{\text{spin}}} + \rho_{J_\varphi^{\text{surf}}}$, where

$$\rho_{J_\varphi^{\text{orb}}} = -f \frac{\epsilon_0 \beta}{4\omega} r |\mathbf{e}|^2 - f \frac{\mu_0 \beta}{4\omega n^2} r |\mathbf{h}|^2,$$

$$\rho_{J_\varphi^{\text{spin}}} = f \frac{\epsilon_0}{2\omega} \text{Im}(e_r e_z^*) + f \frac{\mu_0}{2\omega n^2} \text{Im}(h_r h_z^*),$$

$$\rho_{J_\varphi^{\text{surf}}} = -f \frac{\epsilon_0}{4\omega} \left[r \frac{\partial}{\partial r} \text{Im}(e_r e_z^*) + 3\text{Im}(e_r e_z^*) \right]$$
$$- f \frac{\mu_0}{4\omega n^2} \left[r \frac{\partial}{\partial r} \text{Im}(h_r h_z^*) + 3\text{Im}(h_r h_z^*) \right]. \quad (27)$$

The azimuthal orbital angular momentum density $\rho_{J_\varphi^{\text{orb}}}$ originates from the orbital part S_z^{orb} of the axial component of the Poynting vector. The azimuthal spin and surface angular momentum densities $\rho_{J_\varphi^{\text{spin}}}$ and $\rho_{J_\varphi^{\text{surf}}}$ result from the spin part S_z^{spin} of the axial component of the Poynting vector. Note that the first and second terms in the expressions on the right-hand side of Eqs. (27) correspond to the electric and magnetic parts, respectively. Equations (27) can be used not only for quasicircularly polarized hybrid modes but also for TE and TM modes.

According to Eq. (27), the signs of $\rho_{J_\varphi^{\text{orb}}}$, $\rho_{J_\varphi^{\text{spin}}}$, and $\rho_{J_\varphi^{\text{surf}}}$ depend on the direction of propagation f. The dependence of the local transverse spin density $\rho_{J_\varphi^{\text{spin}}}$ on the direction of propagation is a signature of spin-orbit coupling of light [50–52,71–74]. Note that both $\rho_{J_\varphi^{\text{spin}}}$ and $\rho_{J_\varphi^{\text{surf}}}$ appear as a result of the facts that the longitudinal field components e_z and h_z are nonvanishing and in quadrature with the radial field components e_r and h_r, respectively. It has been shown that, due to spin-orbit coupling of light, spontaneous emission and scattering from an atom with a circular dipole near a nanofiber can be asymmetric with respect to the opposite axial propagation directions [75–80].

VI. HELICITY AND CHIRALITY OF LIGHT

The cycle-averaged optical helicity density of a monochromatic light field is given by [65,81–85]

$$\rho^{\text{hlcy}} = \frac{1}{2c\omega} \text{Im}(\boldsymbol{\mathcal{E}} \cdot \boldsymbol{\mathcal{H}}^*). \quad (28)$$

The helicity of a light beam is closely related to its chirality. Indeed, according to [86], the cycle-averaged optical chirality density of a monochromatic light field can be characterized by the quantity [81,86–90]

$$\rho^{\text{chir}} = \frac{n^2}{2c} \text{Im}[\boldsymbol{\mathcal{E}} \cdot \boldsymbol{\mathcal{H}}^*], \quad (29)$$

so that $\rho^{\text{chir}} = n^2 \omega \rho^{\text{hlcy}}$. Thus, in the frequency domain, the chirality density is proportional to the helicity density and the proportionality factor is $n^2 \omega$.

Note that the optical chirality density (29) can be measured from the asymmetry in the rates of excitation between a small chiral molecule and its mirror image [86,89]. However, according to [91], there is no single measure of chirality. The optical chirality measure (29) is appropriate to chiral effects arising from interference between electric and magnetic dipole transitions [86,89], whereas for chiral effects in spontaneous emission and scattering from atoms with rotating electric dipoles, an appropriate measure of optical chirality is the ellipticity vector of the field polarization [75–80,92].

For quasicircularly polarized hybrid modes, we find the following expression for the helicity density:

$$\rho^{\text{hlcy}} = f p \frac{1}{2c\omega} \text{Im}(e_r h_r^* + e_\varphi h_\varphi^* + e_z h_z^*). \quad (30)$$

The optical helicity per unit length is

$$J^{\text{hlcy}} = \int \rho^{\text{hlcy}} d\mathbf{r}. \quad (31)$$
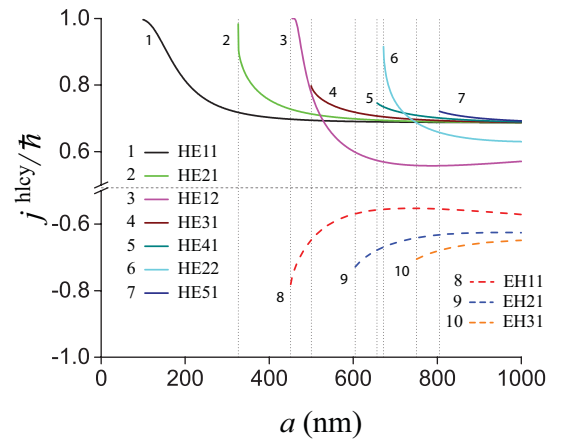
FIG. 22. Helicity per photon j^{hlcy} as a function of the fiber radius a for quasicircularly polarized hybrid modes with the positive propagation direction $f = +$ and the positive phase circulation direction $p = +$. The parameters used are as for Fig. 1. The vertical dotted lines indicate the positions of the cutoffs for higher-order modes. The horizontal dotted line separates the positive and negative sides of the vertical axis.

It is clear from Eqs. (30) and (31) that when we reverse the propagation direction f or the phase circulation direction p, the sign of helicity per unit length is reversed. The explicit expression for the helicity per unit length J^{hlcy} in terms of the fiber parameters is given by Eq. (G3) in Appendix G. Note that the optical helicity of TE and TM guided modes is zero.

The helicity per photon $j^{\text{hlcy}} = \hbar\omega J^{\text{hlcy}}/U$ is shown as a function of the fiber radius a in Fig. 22. One can see that, for the propagation direction $f = +$ and the phase circulation direction $p = +$, the helicity per photon j^{hlcy} is positive for the HE modes and negative for the EH modes. We note that the magnitude of the helicity per photon j^{hlcy} in a guided mode does not exceed the value $\hbar$, which is the value of the helicity per photon of circularly polarized light in free space.

VII. SUMMARY

In this work, we have presented a systematic treatment of higher-order modes of vacuum-clad ultrathin optical fibers. We have shown that, for a given fiber, the higher-order modes have larger penetration lengths, larger effective mode radii, and larger fractional powers outside the fiber than the fundamental mode. We have calculated analytically and numerically the Poynting vector, propagating power, energy, angular momentum, and helicity of the field. In doing so we have shown that the axial component S_z and the azimuthal component S_φ of the Poynting vector can be negative with respect to the direction of propagation and the direction of phase circulation, respectively, depending on the position, the mode type, and the fiber parameters. The occurrence of such a negative axial or azimuthal component of the Poynting vector indicates the possibility of the occurrence of a negative force upon an atom or a small particle. We have also found that the orbital and spin parts of the Poynting vector may have opposite signs in some regions of space. We have shown that, for the EH_{lm} modes with $l = 1,2,\ldots$ and the HE_{lm} modes with $l = 3,4,\ldots$, the limiting values of the fractional power outside the fiber in the cutoff regions are significantly smaller than unity. Meanwhile, for the TE_{0m} and TM_{0m} modes and the HE_{lm} modes with $l = 1$ or 2, the limiting values of the fractional power outside the fiber in the cutoff regions are equal to unity. Our calculations have shown that the angular momentum per photon decreases with increasing fiber radius and increases with increasing azimuthal mode order, and the angular momentum per photon of an EH_{lm} mode is smaller than that of the corresponding HE_{lm} mode. We have found that the orbital part of angular momentum of guided light depends on not only the phase gradient but also the field polarization, and is positive with respect to the direction of the phase circulation axis. Meanwhile, the spin and surface parts of angular momentum and the helicity (chirality) of light in an EH mode are negative with respect to the direction of the phase circulation axis. We have shown that the signs of the orbital, spin, and surface parts of the transverse angular momentum density of the fundamental and higher-order modes depend on the direction of propagation. The directional dependence of the local transverse spin and surface angular momentum densities is a signature of spin-orbit coupling of light and appears as a result of the facts that the longitudinal field components are nonvanishing and in quadrature with the radial

field components. Our results lay the foundations to future research on manipulating and controlling the motion of atoms, molecules, and dielectric particles using higher-order modes of ultrathin fibers.

APPENDIX A: GUIDED MODES OF A STEP-INDEX FIBER

For $l \geqslant 1$, the eigenvalue equation (1) leads to hybrid HE and EH modes [41]. The respective eigenvalue equation is given for the HE modes as

$$\frac{J_{l-1}(ha)}{haJ_l(ha)} = -\frac{n_1^2 + n_2^2}{2n_1^2}\frac{K_l'(qa)}{qaK_l(qa)} + \frac{l}{h^2a^2} - \mathcal{R} \quad (A1)$$

and for the EH modes as

$$\frac{J_{l-1}(ha)}{haJ_l(ha)} = -\frac{n_1^2 + n_2^2}{2n_1^2}\frac{K_l'(qa)}{qaK_l(qa)} + \frac{l}{h^2a^2} + \mathcal{R}. \quad (A2)$$

Here, we have introduced the notation

$$\mathcal{R} = \left[\left(\frac{n_1^2 - n_2^2}{2n_1^2}\right)^2\left(\frac{K_l'(qa)}{qaK_l(qa)}\right)^2 \right.$$
$$\left. + \left(\frac{l\beta}{n_1k}\right)^2\left(\frac{1}{q^2a^2} + \frac{1}{h^2a^2}\right)^2\right]^{1/2}. \quad (A3)$$

For $l = 0$, the eigenvalue equation (1) leads to TE and TM modes [41], with the eigenvalue equation for the TE modes given as

$$\frac{J_1(ha)}{haJ_0(ha)} = -\frac{K_1(qa)}{qaK_0(qa)} \quad (A4)$$

and for the TM modes as

$$\frac{J_1(ha)}{haJ_0(ha)} = -\frac{n_2^2}{n_1^2}\frac{K_1(qa)}{qaK_0(qa)}. \quad (A5)$$

According to [41], the fiber size parameter V is defined as $V = ka\sqrt{n_1^2 - n_2^2}$. The cutoff values V_c for HE_{1m} modes are determined as solutions to the equation $J_1(V_c) = 0$. For HE_{lm} modes with $l = 2,3,\ldots$, the cutoff values are obtained as nonzero solutions to the equation $(n_1^2/n_2^2 + 1)(l - 1)J_{l-1}(V_c) = V_c J_l(V_c)$. The cutoff values V_c for EH_{lm} modes, where $l = 1,2,\ldots$, are determined as nonzero solutions to the equation $J_l(V_c) = 0$. For TE_{0m} and TM_{0m} modes, the cutoff values V_c are obtained as solutions to the equation $J_0(V_c) = 0$.

The electric and magnetic components of the field can be presented in the form

$$\begin{bmatrix}\mathbf{E}\\\mathbf{H}\end{bmatrix} = \frac{1}{2}\begin{bmatrix}\mathcal{E}\\\mathcal{H}\end{bmatrix}e^{-i\omega t} + \text{c.c.}, \quad (A6)$$

where $\mathcal{E}$ and $\mathcal{H}$ are the envelope functions. For a guided mode with a propagation constant β and an azimuthal mode order l,

we can write

$$\begin{bmatrix} \mathcal{E} \\ \mathcal{H} \end{bmatrix} = \begin{bmatrix} \mathbf{e} \\ \mathbf{h} \end{bmatrix} e^{i\beta z + il\varphi}, \tag{A7}$$

where $\mathbf{e}$ and $\mathbf{h}$ are the reduced mode profile functions and β and l can take not only positive but also negative values.

The mode profile functions $\mathbf{e}$ and $\mathbf{h}$ can be decomposed into radial, azimuthal, and axial components denoted by the subscripts r, φ, and z, respectively. We summarize the expressions for the mode functions of hybrid modes, TE modes, and TM modes below [41].

1. Hybrid modes

It is convenient to introduce the parameters

$$s = l\left(\frac{1}{h^2 a^2} + \frac{1}{q^2 a^2}\right)\left[\frac{J_l'(ha)}{ha J_l(ha)} + \frac{K_l'(qa)}{qa K_l(qa)}\right]^{-1},$$

$$s_1 = \frac{\beta^2}{k^2 n_1^2}s, \quad s_2 = \frac{\beta^2}{k^2 n_2^2}s. \tag{A8}$$

Then, we find, for $r < a$,

$$e_r = i A \frac{\beta}{2h}[(1-s)J_{l-1}(hr) - (1+s)J_{l+1}(hr)],$$

$$e_\varphi = -A\frac{\beta}{2h}[(1-s)J_{l-1}(hr) + (1+s)J_{l+1}(hr)], \tag{A9}$$

$$e_z = A J_l(hr),$$

and

$$h_r = A\frac{\omega\epsilon_0 n_1^2}{2h}[(1-s_1)J_{l-1}(hr) + (1+s_1)J_{l+1}(hr)],$$

$$h_\varphi = i A\frac{\omega\epsilon_0 n_1^2}{2h}[(1-s_1)J_{l-1}(hr) - (1+s_1)J_{l+1}(hr)],$$

$$h_z = i A\frac{\beta s}{\omega\mu_0}J_l(hr), \tag{A10}$$

and, for $r > a$,

$$e_r = i A \frac{\beta}{2q}\frac{J_l(ha)}{K_l(qa)}[(1-s)K_{l-1}(qr) + (1+s)K_{l+1}(qr)],$$

$$e_\varphi = -A\frac{\beta}{2q}\frac{J_l(ha)}{K_l(qa)}[(1-s)K_{l-1}(qr) - (1+s)K_{l+1}(qr)],$$

$$e_z = A\frac{J_l(ha)}{K_l(qa)}K_l(qr), \tag{A11}$$

and

$$h_r = A\frac{\omega\epsilon_0 n_2^2}{2q}\frac{J_l(ha)}{K_l(qa)}[(1-s_2)K_{l-1}(qr) - (1+s_2)K_{l+1}(qr)],$$

$$h_\varphi = i A\frac{\omega\epsilon_0 n_2^2}{2q}\frac{J_l(ha)}{K_l(qa)}[(1-s_2)K_{l-1}(qr) + (1+s_2)K_{l+1}(qr)],$$

$$h_z = i A\frac{\beta s}{\omega\mu_0}\frac{J_l(ha)}{K_l(qa)}K_l(qr). \tag{A12}$$

Here, the parameter A is a constant that can be determined from the propagating power of the field.

2. TE modes

For $r < a$, we have

$$e_r = 0, \quad e_\varphi = i\frac{\omega\mu_0}{h}A J_1(hr), \quad e_z = 0, \tag{A13}$$

and

$$h_r = -i\frac{\beta}{h}A J_1(hr), \quad h_\varphi = 0, \quad h_z = A J_0(hr). \tag{A14}$$

For $r > a$, we have

$$e_r = 0, \quad e_\varphi = -i\frac{\omega\mu_0}{q}\frac{J_0(ha)}{K_0(qa)}A K_1(qr), \quad e_z = 0, \tag{A15}$$

and

$$h_r = i\frac{\beta}{q}\frac{J_0(ha)}{K_0(qa)}A K_1(qr), \quad h_\varphi = 0, \quad h_z = \frac{J_0(ha)}{K_0(qa)}A K_0(qr). \tag{A16}$$

3. TM modes

For $r < a$, we have

$$e_r = -i\frac{\beta}{h}A J_1(hr), \quad e_\varphi = 0, \quad e_z = A J_0(hr), \tag{A17}$$

and

$$h_r = 0, \quad h_\varphi = -i\frac{\omega\epsilon_0 n_1^2}{h}A J_1(hr), \quad h_z = 0. \tag{A18}$$

For $r > a$, we have

$$e_r = i\frac{\beta}{q}\frac{J_0(ha)}{K_0(qa)}A K_1(qr), \quad e_\varphi = 0, \quad e_z = \frac{J_0(ha)}{K_0(qa)}A K_0(qr), \tag{A19}$$

and

$$h_r = 0, \quad h_\varphi = i\frac{\omega\epsilon_0 n_2^2}{q}\frac{J_0(ha)}{K_0(qa)}A K_1(qr), \quad h_z = 0. \tag{A20}$$

APPENDIX B: POYNTING VECTOR

In this appendix, we calculate the Poynting vector $\mathbf{S}$ for the different mode families. First we note that, for guided modes of fibers, the radial component of the Poynting vector is always zero, that is, $S_r = 0$.

1. Hybrid modes

For quasicircularly polarized hybrid modes, we find that the axial and azimuthal components of the Poynting vector are given, for $r < a$, by

$$S_z = f|A|^2\frac{\omega\epsilon_0 n_1^2\beta}{4h^2}[(1-s)(1-s_1)J_{l-1}^2(hr)$$
$$+ (1+s)(1+s_1)J_{l+1}^2(hr)],$$

$$S_\varphi = p|A|^2\frac{\omega\epsilon_0 n_1^2}{4h}[(1-2s_1+ss_1)J_{l-1}(hr)J_l(hr)$$
$$+ (1+2s_1+ss_1)J_{l+1}(hr)J_l(hr)], \tag{B1}$$

and, for $r > a$, by

$$
\begin{aligned}
S_z = {}& f|A|^2 \frac{\omega \epsilon_0 n_2^2 \beta}{4q^2} \frac{J_l^2(ha)}{K_l^2(qa)} [(1-s)(1-s_2)K_{l-1}^2(qr) \\
& + (1+s)(1+s_2)K_{l+1}^2(qr)],
\end{aligned}
$$

$$
\begin{aligned}
S_\varphi = {}& p|A|^2 \frac{\omega \epsilon_0 n_2^2}{4q} \frac{J_l^2(ha)}{K_l^2(qa)} [(1-2s_2+ss_2)K_{l-1}(qr)K_l(qr) \\
& - (1+2s_2+ss_2)K_{l+1}(qr)K_l(qr)].
\end{aligned} \tag{B2}
$$

Note that the expressions for S_φ in Eqs. (B1) and (B2) contain cross terms of the types $J_{l\pm1}(hr)J_l(hr)$ and $K_{l\pm1}(qr)K_l(qr)$. These terms appear as a result of the interference between different terms associated with different Bessel functions. Due to the interference, the azimuthal component S_φ of the Poynting vector of a quasicircularly polarized hybrid mode may have different signs in different regions of space.

For quasilinearly polarized hybrid modes, we find that the axial component of the Poynting vector is given, for $r < a$, by

$$
\begin{aligned}
S_z = {}& f|A|^2 \frac{\omega \epsilon_0 n_1^2 \beta}{4h^2} \{(1-s)(1-s_1)J_{l-1}^2(hr) \\
& + (1+s)(1+s_1)J_{l+1}^2(hr) \\
& - 2(1-ss_1)J_{l-1}(hr)J_{l+1}(hr)\cos[2(l\varphi - \varphi_{\mathrm{pol}})]\},
\end{aligned} \tag{B3}
$$

and, for $r > a$, by

$$
\begin{aligned}
S_z = {}& f|A|^2 \frac{\omega \epsilon_0 n_2^2 \beta}{4q^2} \frac{J_l^2(ha)}{K_l^2(qa)} \{(1-s)(1-s_2)K_{l-1}^2(qr) \\
& + (1+s)(1+s_2)K_{l+1}^2(qr) \\
& + 2(1-ss_2)K_{l-1}(qr)K_{l+1}(qr)\cos[2(l\varphi - \varphi_{\mathrm{pol}})]\}. \tag{B4}
\end{aligned}
$$

In both regions, we have $S_\varphi = 0$.

It is worth noting that expressions (B3) and (B4) for S_z contain cross terms of the types $J_{l-1}(hr)J_{l+1}(hr)$ and $K_{l-1}(qr)K_{l+1}(qr)$. A similar argument as the one above confirms that the axial component S_z of the Poynting vector of a quasilinearly polarized hybrid mode can have different signs in different regions of space.

2. TE modes

For TE modes, we find that the axial component of the Poynting vector is given, for $r < a$, by

$$
S_z = f|A|^2 \frac{\omega \mu_0 \beta}{2h^2} J_1^2(hr) \tag{B5}
$$

and, for $r > a$, by

$$
S_z = f|A|^2 \frac{\omega \mu_0 \beta}{2q^2} \frac{J_0^2(ha)}{K_0^2(qa)} K_1^2(qr). \tag{B6}
$$

The azimuthal component is zero, that is, $S_\varphi = 0$. It is clear from Eqs. (B5) and (B6) that, for TE modes, the axial component S_z of the Poynting vector is positive with respect to the direction of propagation, in agreement with the results of Ref. [43].

3. TM modes

For TM modes, we find that the axial component of the Poynting vector is given, for $r < a$, by

$$
S_z = f|A|^2 \frac{\omega \epsilon_0 n_1^2 \beta}{2h^2} J_1^2(hr) \tag{B7}
$$

and, for $r > a$, by

$$
S_z = f|A|^2 \frac{\omega \epsilon_0 n_2^2 \beta}{2q^2} \frac{J_0^2(ha)}{K_0^2(qa)} K_1^2(qr). \tag{B8}
$$

The azimuthal component is zero, that is, $S_\varphi = 0$. It is clear from Eqs. (B7) and (B8) that, for TM modes, the axial component S_z of the Poynting vector is positive with respect to the direction of propagation, in agreement with the results of Ref. [43].

APPENDIX C: POWER

The propagating power of a guided mode is $P = P_{\mathrm{in}} + P_{\mathrm{out}}$, where P_{in} and P_{out} are the propagating powers inside and outside the fiber.

1. Hybrid modes

For hybrid modes, the explicit expressions for the powers inside and outside the fiber are [41,70]

$$
\begin{aligned}
P_{\mathrm{in}} = {}& f|A|^2 \frac{\pi a^2 \omega \epsilon_0 n_1^2 \beta}{4h^2} \{(1-s)(1-s_1)[J_{l-1}^2(ha) \\
& - J_{l-2}(ha)J_l(ha)] + (1+s)(1+s_1)[J_{l+1}^2(ha) \\
& - J_{l+2}(ha)J_l(ha)]\}
\end{aligned} \tag{C1}
$$

and

$$
\begin{aligned}
P_{\mathrm{out}} = {}& f|A|^2 \frac{\pi a^2 \omega \epsilon_0 n_2^2 \beta}{4q^2} \frac{J_l^2(ha)}{K_l^2(qa)} \\
& \times \{(1-s)(1-s_2)[K_{l-2}(qa)K_l(qa) - K_{l-1}^2(qa)] \\
& + (1+s)(1+s_2)[K_{l+2}(qa)K_l(qa) - K_{l+1}^2(qa)]\}. \tag{C2}
\end{aligned}
$$

We consider the asymptotic behavior of P_{out} in the case where the fiber size parameter V is near the cutoff value V_c for a hybrid mode. In the limit $V \to V_c$, we have $qa \to 0$ and $ha \to V_c$.

For EH_{lm} modes, the cutoff value V_c is determined as a nonzero solution to the equation $J_l(V_c) = 0$. In the limit $V \to V_c$ for EH_{lm} modes, the parameters s and s_2 tend to a limiting value s_c, where $s_c \neq -1$. Consequently, the term in the last line of Eq. (C2) is dominant. On the other hand, in the limit $qa \to 0$, we have $K_l(qa) \simeq (1/2)(l-1)!(2/qa)^l$ for $l \geqslant 1$ [93]. With the use of the boundary conditions for the field at the fiber surface, we can show that $J_l(ha) = \mathrm{O}(q^2 a^2)$. When we use the aforementioned asymptotic expressions, we can show that P_{out} tends to a finite value. Meanwhile, P_{in} tends to a nonzero finite value. Consequently, in the limit $V \to V_c$ for EH_{lm} modes, the fractional power outside the fiber η_P tends to a limiting value that is smaller than unity.

For HE_{lm} modes, the cutoff value V_c is not a solution to the equation $J_l(V_c) = 0$ except for the case of $l = 1$. In the

limit $V \to V_c$ for HE$_{lm}$ modes, we have $s = -1 + \mathrm{O}(q^2 a^2)$ and $s_2 = -1 + \mathrm{O}(q^2 a^2)$. When we use these asymptotic expressions and the approximate expression $K_l(qa) \simeq (1/2)(l-1)!(2/qa)^l$ for $l \geqslant 1$ [93], we can show that, for the HE$_{lm}$ modes with $l \geqslant 3$, the power outside the fiber P_{out} tends to a finite value. Meanwhile, P_{in} tends to a nonzero finite value. Consequently, in the limit $V \to V_c$ for the HE$_{lm}$ modes with $l \geqslant 3$, the fractional power outside the fiber η_P tends to a limiting value that is smaller than unity.

The analysis in the above paragraph is not valid for the HE$_{lm}$ modes with $l = 1,2$. Indeed, for $l = 1,2$, the expression on the right-hand side of Eq. (C2) contains the modified Bessel function $K_0(qa)$. The asymptotic expression for this function with a small argument qa is $K_0(qa) \simeq -\ln(qa/2) - \gamma$, where $\gamma \simeq 0.5772$ is the Euler-Mascheroni constant [93]. In addition, for the HE$_{lm}$ modes with $l = 1$, the cutoff value V_c is a solution to the equation $J_1(V_c) = 0$, and the corresponding magnitude of $J_1(ha)$ in the limit $V \to V_c$ is found to be on the order of $1/|\ln qa|$. Then, we can show that, in the limit $V \to V_c$ for the HE$_{lm}$ modes with $l = 1,2$, we have $P_{\mathrm{out}} \to \infty$. Meanwhile, P_{in} tends to a finite value. Consequently, in the limit $V \to V_c$ for the HE$_{lm}$ modes with $l = 1,2$, the fractional power outside the fiber η_P tends to unity.

2. TE modes

For TE modes, the explicit expressions for the powers inside and outside the fiber are [41]

$$P_{\mathrm{in}} = f|A|^2 \frac{\pi a^2 \omega \mu_0 \beta}{2h^2}\big[J_1^2(ha) - J_0(ha)J_2(ha)\big] \quad \text{(C3)}$$

and

$$P_{\mathrm{out}} = f|A|^2 \frac{\pi a^2 \omega \mu_0 \beta}{2q^2} \frac{J_0^2(ha)}{K_0^2(qa)}\big[K_0(qa)K_2(qa) - K_1^2(qa)\big]. \quad \text{(C4)}$$

We calculate the fractional power outside the fiber η_P for a TE mode in the limit where the fiber size parameter V tends to the cutoff value V_c. This cutoff value V_c is determined as a solution to the equation $J_0(V_c) = 0$. In the limit $V \to V_c$, we have $qa \to 0$ and $ha \to V_c$. When we use the eigenvalue equation (A4) for TE modes and the asymptotic expressions for the modified Bessel functions $K_0(qa)$ and $K_1(qa)$ with a small argument qa, we find from Eq. (C4) that $P_{\mathrm{out}} \to \infty$. Meanwhile, P_{in} tends to a finite value. Consequently, in the limit $V \to V_c$ for TE modes, the fractional power outside the fiber η_P tends to unity.

3. TM modes

For TM modes, the explicit expressions for the powers inside and outside the fiber are [41]

$$P_{\mathrm{in}} = f|A|^2 \frac{\pi a^2 \omega \epsilon_0 n_1^2 \beta}{2h^2}\big[J_1^2(ha) - J_0(ha)J_2(ha)\big] \quad \text{(C5)}$$

and

$$P_{\mathrm{out}} = f|A|^2 \frac{\pi a^2 \omega \epsilon_0 n_2^2 \beta}{2q^2} \frac{J_0^2(ha)}{K_0^2(qa)} \\ \times \big[K_0(qa)K_2(qa) - K_1^2(qa)\big]. \quad \text{(C6)}$$

We calculate the fractional power outside the fiber η_P for a TM mode in the limit where the fiber size parameter V tends to the cutoff value V_c. The cutoff value V_c is determined as a solution to the equation $J_0(V_c) = 0$. In the limit $V \to V_c$, we have $qa \to 0$ and $ha \to V_c$. When we use the eigenvalue equation (A5) for TM modes and the asymptotic expressions for the modified Bessel functions $K_0(qa)$ and $K_1(qa)$ with a small argument qa, we find from Eq. (C6) that $P_{\mathrm{out}} \to \infty$. Meanwhile, P_{in} tends to a finite value. Consequently, in the limit $V \to V_c$ for TM modes, the fractional power outside the fiber η_P tends to unity.

APPENDIX D: ENERGY PER UNIT LENGTH

The energy per unit length of a guided mode is $U = U_{\mathrm{in}} + U_{\mathrm{out}}$, where U_{in} and U_{out} are the energies per unit length inside and outside the fiber.

1. Hybrid modes

For hybrid modes, the explicit expressions for the energies per unit length inside and outside the fiber are found to be [41,70]

$$\begin{aligned} U_{\mathrm{in}} = |A|^2 \frac{\pi a^2 \epsilon_0 n_1^2}{4} \bigg\{ & \frac{1}{2h^2}\big[\beta^2(1-s)^2 + n_1^2 k^2(1-s_1)^2\big] \\ & \times \big[J_{l-1}^2(ha) - J_{l-2}(ha)J_l(ha)\big] \\ & + \frac{1}{2h^2}\big[\beta^2(1+s)^2 + n_1^2 k^2(1+s_1)^2\big] \\ & \times \big[J_{l+1}^2(ha) - J_{l+2}(ha)J_l(ha)\big] \\ & + \bigg(1 + \frac{\beta^2 s^2}{n_1^2 k^2}\bigg)\big[J_l^2(ha) - J_{l-1}(ha)J_{l+1}(ha)\big] \bigg\} \end{aligned} \quad \text{(D1)}$$

and

$$\begin{aligned} U_{\mathrm{out}} = |A|^2 \frac{\pi a^2 \epsilon_0 n_2^2}{4} \frac{J_l^2(ha)}{K_l^2(qa)} \bigg\{ & \frac{1}{2q^2}\big[\beta^2(1-s)^2 \\ & + n_2^2 k^2(1-s_2)^2\big]\big[K_{l-2}(qa)K_l(qa) - K_{l-1}^2(qa)\big] \\ & + \frac{1}{2q^2}\big[\beta^2(1+s)^2 + n_2^2 k^2(1+s_2)^2\big] \\ & \times \big[K_{l+2}(qa)K_l(qa) - K_{l+1}^2(qa)\big] \\ & + \bigg(1 + \frac{\beta^2 s^2}{n_2^2 k^2}\bigg)\big[K_{l-1}(qa)K_{l+1}(qa) - K_l^2(qa)\big] \bigg\}. \end{aligned} \quad \text{(D2)}$$

2. TE modes

For TE modes, the explicit expressions for the energies per unit length inside and outside the fiber are found to be

$$\begin{aligned} U_{\mathrm{in}} = |A|^2 \frac{\pi a^2 \mu_0}{4}\bigg[& J_0^2(ha) + \frac{2n_1^2 k^2}{h^2} J_1^2(ha) \\ & + \bigg(1 - \frac{2n_1^2 k^2}{h^2}\bigg) J_0(ha)J_2(ha)\bigg] \end{aligned} \quad \text{(D3)}$$

and

$$U_{\text{out}} = |A|^2 \frac{\pi a^2 \mu_0}{4} \frac{J_0^2(ha)}{K_0^2(qa)} \left\{ \left(1 + \frac{2n_2^2 k^2}{q^2}\right) K_0(qa) K_2(qa) \right.$$
$$\left. - \frac{2n_2^2 k^2}{q^2} K_1^2(qa) - K_0^2(qa) \right\}. \quad (D4)$$

3. TM modes

For TM modes, the explicit expressions for the energies per unit length inside and outside the fiber are found to be

$$U_{\text{in}} = |A|^2 \frac{\pi a^2 \epsilon_0 n_1^2}{4} \left[J_0^2(ha) + \frac{2n_1^2 k^2}{h^2} J_1^2(ha) \right.$$
$$\left. + \left(1 - \frac{2n_1^2 k^2}{h^2}\right) J_0(ha) J_2(ha) \right] \quad (D5)$$

and

$$U_{\text{out}} = |A|^2 \frac{\pi a^2 \epsilon_0 n_2^2}{4} \frac{J_0^2(ha)}{K_0^2(qa)} \left[\left(1 + \frac{2n_2^2 k^2}{q^2}\right) K_0(qa) K_2(qa) \right.$$
$$\left. - \frac{2n_2^2 k^2}{q^2} K_1^2(qa) - K_0^2(qa) \right]. \quad (D6)$$

APPENDIX E: DECOMPOSITION OF THE POYNTING VECTOR

We decompose the Poynting vector into the orbital and spin parts.

1. Hybrid modes

We consider quasicircularly polarized hybrid modes. For the electric components of the orbital and spin parts of the Poynting vector, we find the expressions

$$S_z^{\text{e-orb}} = f \frac{c\epsilon_0 \beta}{4k} |\mathbf{e}|^2,$$
$$S_\varphi^{\text{e-orb}} = p \frac{c\epsilon_0}{4kr} [l|\mathbf{e}|^2 + 2\text{Im}(e_r e_\varphi^*)], \quad (E1)$$

and

$$S_z^{\text{e-spin}} = f \frac{c\epsilon_0}{4kr} \frac{\partial}{\partial r} [r\text{Im}(e_r e_z^*)],$$
$$S_\varphi^{\text{e-spin}} = p \frac{c\epsilon_0}{4k} \frac{\partial}{\partial r} \text{Im}(e_r e_\varphi^*). \quad (E2)$$

We note that, in the case where $l = 1$, Eqs. (E1) and (E2) reduce to the results of Ref. [26] for the orbital and spin parts of the Poynting vector of the fundamental HE$_{11}$ mode.

For the magnetic components of the orbital and spin parts of the Poynting vector, we find the expressions

$$S_z^{\text{h-orb}} = f \frac{c\mu_0 \beta}{4kn^2} |\mathbf{h}|^2,$$
$$S_\varphi^{\text{h-orb}} = p \frac{c\mu_0}{4kn^2 r} [l|\mathbf{h}|^2 + 2\text{Im}(h_r h_\varphi^*)], \quad (E3)$$

and

$$S_z^{\text{h-spin}} = f \frac{c\mu_0}{4kn^2 r} \frac{\partial}{\partial r} [r\text{Im}(h_r h_z^*)],$$
$$S_\varphi^{\text{h-spin}} = p \frac{c\mu_0}{4kn^2} \frac{\partial}{\partial r} \text{Im}(h_r h_\varphi^*). \quad (E4)$$

Equations (E1) and (E3) show that the orbital parts of the axial and azimuthal components of the Poynting vector are positive with respect to the direction of propagation and the direction of phase circulation, respectively.

Equations (E2) and (E4) show that the signs of the spin parts of the axial and azimuthal components of the Poynting vector can vary in the fiber transverse plane. Thus, the spin parts of the axial and azimuthal components of the Poynting vector may be negative with respect to the direction of propagation and the direction of phase circulation, respectively. Consequently, the orbital and spin parts of the Poynting vector may have opposite signs.

The first expressions in Eqs. (E1) and (E3) indicate that the orbital part of the axial component of the Poynting vector is determined by the local density of energy.

Meanwhile, the second expressions in Eqs. (E1) and (E3) contain not only the terms $l|\mathbf{e}|^2$ and $l|\mathbf{h}|^2$, which result from the local phase gradient, but also the terms $\text{Im}(e_r e_\varphi^*)$ and $\text{Im}(h_r h_\varphi^*)$, which result from the local polarization. This indicates that the orbital part of the azimuthal component of the Poynting vector of a hybrid mode depends on not only the local phase gradient but also the local polarization, unlike the case of uniformly polarized paraxial beams [52].

2. TE modes

We consider TE modes. For the fields in these modes, the Poynting vector is aligned along the z axis. For the electric components of the orbital and spin parts of the Poynting vector, we find the expressions

$$S_z^{\text{e-orb}} = f \frac{c\epsilon_0 \beta}{4k} |\mathbf{e}|^2, \quad S_z^{\text{e-spin}} = 0, \quad (E5)$$

and $S_\varphi^{\text{e-orb}} = S_\varphi^{\text{e-spin}} = 0$.

For the magnetic components of the orbital and spin parts of the Poynting vector, we find the expressions

$$S_z^{\text{h-orb}} = f \frac{c\mu_0 \beta}{4kn^2} |\mathbf{h}|^2, \quad S_z^{\text{h-spin}} = f \frac{c\mu_0}{4kn^2 r} \frac{\partial}{\partial r} [r\text{Im}(h_r h_z^*)], \quad (E6)$$

and $S_\varphi^{\text{h-orb}} = S_\varphi^{\text{h-spin}} = 0$.

It is clear that the orbital part of the axial component of the Poynting vector of a TE mode is determined by the local density of energy and is positive with respect to the direction of propagation.

3. TM modes

We consider TM modes. For the fields in these modes, the Poynting vector is aligned along the z axis. For the electric components of the orbital and spin parts of the Poynting vector, we find the expressions

$$S_z^{\text{e-orb}} = f \frac{c\epsilon_0 \beta}{4k} |\mathbf{e}|^2, \quad S_z^{\text{e-spin}} = f \frac{c\epsilon_0}{4kr} \frac{\partial}{\partial r} [r\text{Im}(e_r e_z^*)], \quad (E7)$$

and $S_\varphi^{\text{e-orb}} = S_\varphi^{\text{e-spin}} = 0$.

For the magnetic components of the orbital and spin parts of the Poynting vector, we find the expressions

$$S_z^{\text{h-orb}} = f \frac{c\mu_0\beta}{4kn^2}|\mathbf{h}|^2, \quad S_z^{\text{h-spin}} = 0, \tag{E8}$$

and $S_\varphi^{\text{h-orb}} = S_\varphi^{\text{h-spin}} = 0$.

It is clear that the orbital part of the axial component of the Poynting vector of a TM mode is determined by the local density of energy and is positive with respect to the direction of propagation.

APPENDIX F: ANGULAR MOMENTUM AND DECOMPOSITION

We consider quasicircularly polarized hybrid modes. The angular momentum of light per unit length of a quasicircularly polarized hybrid mode is aligned along the fiber axis z and is given by $J_z = J_z^{\text{in}} + J_z^{\text{out}}$. Here, J_z^{in} and J_z^{out} are the parts of the angular momentum per unit length inside and outside the fiber. The explicit expressions for J_z^{in} and J_z^{out} are found to be

$$J_z^{\text{in}} = p|A|^2 \frac{\pi a^2 \omega \epsilon_0 n_1^2}{2h^2 c^2} \left\{ l(1 + ss_1)J_l^2(ha) - [l(1 + ss_1) + 2s_1]J_{l-1}(ha)J_{l+1}(ha) \right\} \tag{F1}$$

and

$$J_z^{\text{out}} = p|A|^2 \frac{\pi a^2 \omega \epsilon_0 n_2^2}{2q^2 c^2} \frac{J_l^2(ha)}{K_l^2(qa)} \left\{ l(1 + ss_2)K_l^2(qa) - [l(1 + ss_2) + 2s_2]K_{l-1}(qa)K_{l+1}(qa) \right\}, \tag{F2}$$

and we note that, for $l = 1$, Eqs. (F1) and (F2) reduce to the results of Ref. [70] for the angular momentum of the fundamental HE_{11} mode.

The angular momentum per unit length J_z can be decomposed as $J_z = J_z^{\text{orb}} + J_z^{\text{spin}} + J_z^{\text{surf}}$. Here, J_z^{orb}, J_z^{spin}, and J_z^{surf} are given by Eqs. (24)–(26), respectively, and are interpreted as the orbital, spin, and surface parts [58–60,62]. In the dual-symmetric formalism, we have $J_z^{\text{orb}} = J_z^{\text{e-orb}} + J_z^{\text{h-orb}}$, $J_z^{\text{spin}} = J_z^{\text{e-spin}} + J_z^{\text{h-spin}}$, and $J_z^{\text{surf}} = J_z^{\text{e-surf}} + J_z^{\text{h-surf}}$. Here, the terms with the letters e and h in the superscripts correspond to the first and second terms, respectively, in Eqs. (24)–(26), and are called the electric and magnetic components.

For the electric and magnetic components of the orbital angular momentum, we find the explicit expressions

$$J_z^{\text{e-orb}} = pl|A|^2 \frac{\pi a^2 \epsilon_0}{8h^2 \omega} \left\{ \beta^2(1-s)^2 \left[J_{l-1}^2(ha) - J_{l-2}(ha)J_l(ha) \right] + \beta^2(1+s)^2 \left[J_{l+1}^2(ha) - J_{l+2}(ha)J_l(ha) \right] \right.$$
$$\left. + 2h^2 \left[J_l^2(ha) - J_{l-1}(ha)J_{l+1}(ha) \right] \right\} + pl|A|^2 \frac{\pi a^2 \epsilon_0}{8q^2 \omega} \frac{J_l^2(ha)}{K_l^2(qa)} \left\{ \beta^2(1-s)^2 \left[K_{l-2}(qa)K_l(qa) - K_{l-1}^2(qa) \right] \right.$$
$$\left. + \beta^2(1+s)^2 \left[K_{l+2}(qa)K_l(qa) - K_{l+1}^2(qa) \right] + 2q^2 \left[K_{l-1}(qa)K_{l+1}(qa) - K_l^2(qa) \right] \right\} - J_z^{\text{e-spin}} \tag{F3}$$

and

$$J_z^{\text{h-orb}} = pl|A|^2 \frac{\pi a^2 \epsilon_0 n_1^2 k}{8h^2 \beta^2 c} \left\{ \beta^2(1-s_1)^2 \left[J_{l-1}^2(ha) - J_{l-2}(ha)J_l(ha) \right] + \beta^2(1+s_1)^2 \left[J_{l+1}^2(ha) - J_{l+2}(ha)J_l(ha) \right] \right.$$
$$\left. + 2h^2 s_1^2 \left[J_l^2(ha) - J_{l-1}(ha)J_{l+1}(ha) \right] \right\} + pl|A|^2 \frac{\pi a^2 \epsilon_0 n_2^2 k}{8q^2 \beta^2 c} \frac{J_l^2(ha)}{K_l^2(qa)} \left\{ \beta^2(1-s_2)^2 \left[K_{l-2}(qa)K_l(qa) - K_{l-1}^2(qa) \right] \right.$$
$$\left. + \beta^2(1+s_2)^2 \left[K_{l+2}(qa)K_l(qa) - K_{l+1}^2(qa) \right] + 2q^2 s_2^2 \left[K_{l-1}(qa)K_{l+1}(qa) - K_l^2(qa) \right] \right\} - J_z^{\text{h-spin}}. \tag{F4}$$

For the electric and magnetic components of the spin angular momentum, we find the explicit expressions

$$J_z^{\text{e-spin}} = p|A|^2 \frac{\pi a^2 \epsilon_0 \beta^2}{8h^2 \omega} \left\{ (1-s)^2 \left[J_{l-1}^2(ha) - J_{l-2}(ha)J_l(ha) \right] - (1+s)^2 \left[J_{l+1}^2(ha) - J_{l+2}(ha)J_l(ha) \right] \right\}$$
$$+ p|A|^2 \frac{\pi a^2 \epsilon_0 \beta^2}{8q^2 \omega} \frac{J_l^2(ha)}{K_l^2(qa)} \left\{ (1-s)^2 \left[K_{l-2}(qa)K_l(qa) - K_{l-1}^2(qa) \right] - (1+s)^2 \left[K_{l+2}(qa)K_l(qa) - K_{l+1}^2(qa) \right] \right\} \tag{F5}$$

and

$$J_z^{\text{h-spin}} = p|A|^2 \frac{\pi a^2 \epsilon_0 n_1^2 k}{8h^2 c} \left\{ (1-s_1)^2 \left[J_{l-1}^2(ha) - J_{l-2}(ha)J_l(ha) \right] - (1+s_1)^2 \left[J_{l+1}^2(ha) - J_{l+2}(ha)J_l(ha) \right] \right\}$$
$$+ p|A|^2 \frac{\pi a^2 \epsilon_0 n_2^2 k}{8q^2 c} \frac{J_l^2(ha)}{K_l^2(qa)} \left\{ (1-s_2)^2 \left[K_{l-2}(qa)K_l(qa) - K_{l-1}^2(qa) \right] - (1+s_2)^2 \left[K_{l+2}(qa)K_l(qa) - K_{l+1}^2(qa) \right] \right\}. \tag{F6}$$

In the particular case where $l = 1$, Eq. (F5) reduces to the result of Ref. [70] for the spin angular momentum of the fundamental HE_{11} mode.

For the electric and magnetic components of the surface angular momentum, we find the explicit expressions

$$J_z^{\text{e-surf}} = p|A|^2 \frac{\pi a^2 \epsilon_0 \beta^2}{8h^2 \omega} \left(\frac{n_1^2}{n_2^2} - 1 \right) \left[(1-s)^2 J_{l-1}^2(ha) - (1+s)^2 J_{l+1}^2(ha) \right] \tag{F7}$$

and

$$J_z^{\text{h-surf}} = p|A|^2 \frac{\pi a^2 \epsilon_0 n_1^2 k}{8h^2 c} \left(\frac{n_1^2}{n_2^2} - 1 \right) \left[(1-s_1)^2 J_{l-1}^2(ha) - (1+s_1)^2 J_{l+1}^2(ha) \right]. \tag{F8}$$

APPENDIX G: HELICITY AND CHIRALITY OF GUIDED LIGHT

We calculate the helicity and chirality of guided light. The cycle-averaged optical helicity density of a monochromatic field is given by [65,81–85]

$$\rho^{\text{hlcy}} = \frac{1}{4c} \text{Re}(\mathcal{A} \cdot \mathcal{H}^*) - \frac{\epsilon_0 n^2}{4} \text{Re}(\mathcal{C} \cdot \mathcal{E}^*), \tag{G1}$$

where $\mathcal{A}$ and $\mathcal{C}$ are the positive-frequency components of the magnetic and electric vector potentials. With the help of the relations $\mathcal{A} = \mathcal{E}/i\omega$ and $n^2 \mathcal{C} = \mu_0 c \mathcal{H}/i\omega$, we can then obtain Eq. (28) (see [65,81–85]).

Helicity of a light beam is closely related to its chirality. Indeed, according to [86], the cycle-averaged optical chirality density of a monochromatic field is characterized by the quantity [81,86–90]

$$\rho^{\text{chir}} = \frac{c\epsilon_0 n^2}{4\omega} \text{Re}[\mathcal{E}^* \cdot (\nabla \times \mathcal{E})] + \frac{c\mu_0}{4\omega} \text{Re}[\mathcal{H}^* \cdot (\nabla \times \mathcal{H})]. \tag{G2}$$

When we use the equations $\nabla \times \mathcal{E} = i\omega\mu_0 \mathcal{H}$ and $\nabla \times \mathcal{H} = -i\omega\epsilon_0 n^2 \mathcal{E}$, we obtain Eq. (29) (see [88]).

The optical helicity per unit length J^{hlcy} is given by Eq. (31). For quasicircularly polarized hybrid modes, the explicit expression for the helicity per unit length is found to be

$$\begin{aligned}
J^{\text{hlcy}} = {} & fp|A|^2 \frac{\pi a^2 \epsilon_0 \beta}{4h^2 k^2 c} \left\{ n_1^2 k^2 (1-s)(1-s_1) \left[J_{l-1}^2(ha) - J_{l-2}(ha)J_l(ha) \right] - n_1^2 k^2 (1+s)(1+s_1) \left[J_{l+1}^2(ha) - J_{l+2}(ha)J_l(ha) \right] \right. \\
& \left. - 2h^2 s \left[J_l^2(ha) - J_{l+1}(ha)J_{l-1}(ha) \right] \right\} + fp|A|^2 \frac{\pi a^2 \epsilon_0 \beta}{4q^2 k^2 c} \frac{J_l^2(ha)}{K_l^2(qa)} \left\{ n_2^2 k^2 (1-s)(1-s_2) \left[K_{l-2}(qa)K_l(qa) - K_{l-1}^2(qa) \right] \right. \\
& \left. - n_2^2 k^2 (1+s)(1+s_2) \left[K_{l+2}(qa)K_l(qa) - K_{l+1}^2(qa) \right] - 2q^2 s \left[K_{l+1}(qa)K_{l-1}(qa) - K_l^2(qa) \right] \right\}. \tag{G3}
\end{aligned}$$

[1] L. Tong, R. R. Gattass, J. B. Ashcom, S. He, J. Lou, M. Shen, I. Maxwell, and E. Mazur, Nature (London) **426**, 816 (2003).

[2] T. A. Birks, W. J. Wadsworth, and P. St. J. Russell, Opt. Lett. **25**, 1415 (2000); S. G. Leon-Saval, T. A. Birks, W. J. Wadsworth, P. St. J. Russell, and M. W. Mason, in *Conference on Lasers and Electro-Optics (CLEO), Technical Digest*, postconference ed. (Optical Society of America, Washington, DC, 2004), paper CPDA6.

[3] J. C. Knight, G. Cheung, F. Jacques, and T. A. Birks, Opt. Lett. **22**, 1129 (1997); M. Cai and K. Vahala, *ibid.* **26**, 884 (2001).

[4] J. M. Ward, A. Maimaiti, V. H. Le, and S. Nic Chormaic, Rev. Sci. Instrum. **85**, 111501 (2014).

[5] J. Bures and R. Ghosh, J. Opt. Soc. Am. A **16**, 1992 (1999).

[6] L. Tong, J. Lou, and E. Mazur, Opt. Express **12**, 1025 (2004).

[7] Fam Le Kien, J. Q. Liang, K. Hakuta, and V. I. Balykin, Opt. Commun. **242**, 445 (2004).

[8] M. J. Morrissey, K. Deasy, M. Frawley, R. Kumar, E. Prel, L. Russell, V. G. Truong, and S. Nic Chormaic, Sensors **13**, 10449 (2013).

[9] T. Nieddu, V. Gokhroo, and S. Nic Chormaic, J. Opt. **18**, 053001 (2016).

[10] V. I. Balykin, K. Hakuta, Fam Le Kien, J. Q. Liang, and M. Morinaga, Phys. Rev. A **70**, 011401(R) (2004); Fam Le Kien, V. I. Balykin, and K. Hakuta, *ibid.* **70**, 063403 (2004).

[11] E. Vetsch, D. Reitz, G. Sagué, R. Schmidt, S. T. Dawkins, and A. Rauschenbeutel, Phys. Rev. Lett. **104**, 203603 (2010).

[12] A. Goban, K. S. Choi, D. J. Alton, D. Ding, C. Lacroûte, M. Pototschnig, T. Thiele, N. P. Stern, and H. J. Kimble, Phys. Rev. Lett. **109**, 033603 (2012).

[13] P. Domokos, P. Horak, and H. Ritsch, Phys. Rev. A **65**, 033832 (2002).

[14] Fam Le Kien, V. I. Balykin, and K. Hakuta, Phys. Rev. A **73**, 013819 (2006).

[15] K. P. Nayak, P. N. Melentiev, M. Morinaga, Fam Le Kien, V. I. Balykin, and K. Hakuta, Opt. Express **15**, 5431 (2007).

[16] K. P. Nayak, Fam Le Kien, M. Morinaga, and K. Hakuta, Phys. Rev. A **79**, 021801(R) (2009).

[17] S. T. Dawkins, R. Mitsch, D. Reitz, E. Vetsch, and A. Rauschenbeutel, Phys. Rev. Lett. **107**, 243601 (2011).

[18] D. Reitz, C. Sayrin, R. Mitsch, P. Schneeweiss, and A. Rauschenbeutel, Phys. Rev. Lett. **110**, 243603 (2013).

[19] L. Russell, R. Kumar, V. B. Tiwari, and S. Nic Chormaic, Opt. Commun. **309**, 313 (2013).

[20] A. Stiebeiner, O. Rehband, R. Garcia-Fernandez, and A. Rauschenbeutel, Opt. Express **17**, 21704 (2009).

[21] R. Yalla, Fam Le Kien, M. Morinaga, and K. Hakuta, Phys. Rev. Lett. **109**, 063602 (2012).

[22] T. Schröder, M. Fujiwara, T. Noda, H.-Q. Zhao, O. Benson, and S. Takeuchi, Opt. Express **20**, 10490 (2012).

[23] L. Liebermeister, F. Petersen, A. V. Münchow, D. Burchardt, J. Hermelbracht, T. Tashima, A. W. Schell, O. Benson, T. Meinhardt, A. Krueger, A. Stiebeiner, A. Rauschenbeutel, H. Weinfurter, and M. Weber, Appl. Phys. Lett. **104**, 031101 (2014).

[24] G. Brambilla, G. S. Murugan, J. S. Wilkinson, and D. J. Richardson, Opt. Lett. **32**, 3041 (2007).

[25] S. E. Skelton, M. Sergides, R. Patel, E. Karczewska, O. M. Maragó, and P. H. Jones, J. Quant. Spectrosc. Radiat. Transfer **113**, 2512 (2012).

[26] Fam Le Kien and A. Rauschenbeutel, Phys. Rev. A **88**, 063845 (2013).

[27] J. Fu, X. Yin, and L. Tong, J. Phys. B: At. Mol. Opt. Phys. **40**, 4195 (2007).

[28] G. Sagué, A. Baade, and A. Rauschenbeutel, New J. Phys. **10**, 113008 (2008).

[29] J. Fu, X. Yin, N. Li, and L. Tong, Chin. Opt. Lett. **6**, 112 (2008).

[30] A. V. Masalov and V. G. Minogin, Laser Phys. Lett. **10**, 075203 (2013).

[31] C. F. Phelan, T. Hennessy, and Th. Busch, Opt. Express **21**, 27093 (2013).

[32] M. Sadgrove, S. Wimberger, and S. Nic Chormaic, Sci. Rep. **6**, 28905 (2016).

[33] M. H. Alizadeh and B. M. Reinhard, Opt. Lett. **41**, 4735 (2016).

[34] G. Volpe and D. Petrov, Opt. Commun. **237**, 89 (2004).

[35] A. Petcu-Colan, M. Frawley, and S. Nic Chormaic, J. Nonlinear Opt. Phys. Mater. **20**, 293 (2011).

[36] M. C. Frawley, A. Petcu-Colan, V. G. Truong, and S. Nic Chormaic, Opt. Commun. **285**, 4648 (2012).

[37] S. Ravets, J. E. Hoffman, L. A. Orozco, S. L. Rolston, G. Beadie, and F. K. Fatemi, Opt. Express **21**, 18325 (2013).

[38] R. Kumar, V. Gokhroo, K. Deasy, A. Maimaiti, M. C. Frawley, C. Phelan, and S. Nic Chormaic, New J. Phys. **17**, 013026 (2015).

[39] A. Maimaiti, V. G. Truong, M. Sergides, I. Gusachenko, and S. Nic Chormaic, Sci. Rep. **5**, 09077 (2015).

[40] A. Maimaiti, D. Holzmann, V. G. Truong, H. Ritsch, and S. Nic Chormaic, Sci. Rep. **6**, 30131 (2016).

[41] See, for example, D. Marcuse, *Light Transmission Optics* (Krieger, Malabar, 1989); A. W. Snyder and J. D. Love, *Optical Waveguide Theory* (Chapman and Hall, New York, 1983); K. Okamoto, *Fundamentals of Optical Waveguides* (Elsevier, New York, 2006).

[42] Y. Roichman, B. Sun, Y. Roichman, J. Amato-Grill, and D. G. Grier, Phys. Rev. Lett. **100**, 013602 (2008).

[43] S. Mokhov, R. El-Ganainy, and D. N. Christodoulides, Opt. Express **14**, 3255 (2006).

[44] A. V. Novitsky and D. V. Novitsky, J. Opt. Soc. Am. A **24**, 2844 (2007).

[45] A. Maimaiti, Ph.D. thesis, National University of Ireland, 2016.

[46] M. V. Berry, J. Opt. A: Pure Appl. Opt. **11**, 094001 (2009).

[47] A. Bekshaev, K. Y. Bliokh, and M. Soskin, J. Opt. **13**, 053001 (2011).

[48] K. Y. Bliokh and F. Nori, Phys. Rev. A **85**, 061801(R) (2012).

[49] K. Y. Bliokh, A. Y. Bekshaev, and F. Nori, New J. Phys. **15**, 033026 (2013).

[50] K. Y. Bliokh, J. Dressel, and F. Nori, New J. Phys. **16**, 093037 (2014).

[51] K. Y. Bliokh, A. Y. Bekshaev, and F. Nori, Nat. Commun. **5**, 3300 (2014).

[52] K. Y. Bliokh and F. Nori, Phys. Rep. **592**, 1 (2015).

[53] See, for example, J. D. Jackson, *Classical Electrodynamics*, 3rd ed. (Wiley, New York, 1999).

[54] I. Brevik, Phys. Rep. **52**, 133 (1979).

[55] M. Abraham, Rend. Circ. Mat. Palermo **28**, 1 (1909); **30**, 33 (1910).

[56] H. Minkowski, Math. Ann. **68**, 472 (1910) [Nachr. Ges. Wiss. Goettingen, p. 53 (1908)].

[57] M. Padgett, S. M. Barnett, and R. Loudon, J. Mod. Opt. **50**, 1555 (2003).

[58] C. Cohen-Tannoudji, J. Dupont-Roc, and G. Grynberg, *Photons and Atoms* (Wiley, New York, 2004), Chap. I.

[59] J. Humblet, Physica **10**, 585 (1943).

[60] S. M. Barnett and L. Allen, Opt. Commun. **110**, 670 (1994).

[61] J. B. Götte and S. M. Barnett, in *The Angular Momentum of Light*, edited by D. L. Andrews and M. Babiker (Cambridge University Press, New York, 2012), p. 1.

[62] M. Ornigotti and A. Aiello, Opt. Express **22**, 6586 (2014).

[63] L. Allen, M. J. Padgett, and M. Babiker, Prog. Opt. **39**, 291 (1999), and references therein.

[64] L. Mandel and E. Wolf, *Optical Coherence and Quantum Optics* (Cambridge University Press, New York, 1995), p. 488.

[65] R. P. Cameron, S. M. Barnett, and A. M. Yao, New J. Phys. **14**, 053050 (2012).

[66] *Optical Orbital Angular Momentum*, edited by S. M. Barnett, M. Babiker, and M. J. Padgett, Philos. Trans. R. Soc. London A **375**, 20150444 (2017).

[67] L. Allen, M. W. Beijersbergen, R. J. C. Spreeuw, and J. P. Woerdman, Phys. Rev. A **45**, 8185 (1992).

[68] L. Allen and M. J. Padgett, Opt. Commun. **184**, 67 (2000).

[69] C. Maurer, A. Jesacher, S. Fürhapter, S. Bernet, and M. Ritsch-Marte, New J. Phys. **9**, 78 (2007).

[70] Fam Le Kien, V. I. Balykin, and K. Hakuta, Phys. Rev. A **73**, 053823 (2006).

[71] A. V. Dooghin, N. D. Kundikova, V. S. Liberman, and B. Y. Zeldovich, Phys. Rev. A **45**, 8204 (1992); V. S. Liberman and B. Y. Zeldovich, *ibid.* **46**, 5199 (1992); M. Y. Darsht, B. Y. Zeldovich, I. V. Kataevskaya, and N. D. Kundikova, JETP **80**, 817 (1995) [Zh. Eksp. Theor. Phys. **107**, 1464 (1995)].

[72] K. Y. Bliokh, A. Aiello, and M. A. Alonso, in *The Angular Momentum of Light*, edited by D. L. Andrews and M. Babiker (Cambridge University Press, New York, 2012), p. 174.

[73] A. Aiello, P. Banzer, M. Neugebauer, and G. Leuchs, Nat. Photon. **9**, 789 (2015).

[74] K. Y. Bliokh, F. J. Rodriguez-Fortuño, F. Nori, and A. V. Zayats, Nat. Photon. **9**, 796 (2015).

[75] Fam Le Kien and A. Rauschenbeutel, Phys. Rev. A **90**, 023805 (2014).

[76] J. Petersen, J. Volz, and A. Rauschenbeutel, Science **346**, 67 (2014).

[77] R. Mitsch, C. Sayrin, B. Albrecht, P. Schneeweiss, and A. Rauschenbeutel, Nat. Commun. **5**, 5713 (2014).

[78] Fam Le Kien and A. Rauschenbeutel, Phys. Rev. A **90**, 063816 (2014).

[79] C. Sayrin, C. Junge, R. Mitsch, B. Albrecht, D. O'Shea, P. Schneeweiss, J. Volz, and A. Rauschenbeutel, Phys. Rev. X **5**, 041036 (2015).

[80] P. Lodahl, S. Mahmoodian, S. Stobbe, P. Schneeweiss, J. Volz, A. Rauschenbeutel, H. Pichler, and P. Zoller, Nature (London) **541**, 473 (2017).

[81] G. Nienhuis, Phys. Rev. A **93**, 023840 (2016).

[82] D. J. Candlin, Nuovo Cimento **37**, 1390 (1965).

[83] J. L. Trueba and A. F. Ranada, Eur. J. Phys. **17**, 141 (1996).

[84] G. N. Afanasiev and Y. P. Stepanovsky, Nuovo Cimento A **109**, 271 (1996).

[85] T. G. Philbin, Phys. Rev. A **87**, 043843 (2013).

[86] Y. Tang and A. E. Cohen, Phys. Rev. Lett. **104**, 163901 (2010).

[87] D. Lipkin, J. Math. Phys. **5**, 696 (1964).

[88] K. Y. Bliokh and F. Nori, Phys. Rev. A **83**, 021803 (2011).

[89] Y. Tang and A. E. Cohen, Science **332**, 333 (2011).

[90] M. M. Coles and D. L. Andrews, Phys. Rev. A **85**, 063810 (2012).

[91] A. B. Harris, R. D. Kamien, and T. C. Lubensky, Rev. Mod. Phys. **71**, 1745 (1999).

[92] Fam Le Kien and A. Rauschenbeutel, Phys. Rev. A **93**, 043828 (2016).

[93] *Handbook of Mathematical Functions*, edited by M. Abramowitz and I. A. Stegun (Dover, New York, 2013).